POLITECNICO DI TORINO
Repository ISTITUZIONALE

Degradation of Anion Exchange Membrane Water Electrolyzers Under Shutdown and Open-Circuit Transients: Protocols, Mechanisms, Diagnostics, and Mitigation

Original
Degradation of Anion Exchange Membrane Water Electrolyzers Under Shutdown and Open-Circuit Transients: Protocols, Mechanisms, Diagnostics, and Mitigation / Rahman, M.M., Santarelli, M.. - In: HYDROGEN. - ISSN 2673-4141. - 7:4(2026). [10.3390/hydrogen7040195]

Availability:
This version is available at: 11583/3018168 since: 2026-11-19T15:38:06Z

Publisher:
MDPI

Published
DOI:10.3390/hydrogen7040195

Terms of use:

This article is made available under terms and conditions as specified in the corresponding bibliographic description in the repository

Publisher copyright

(Article begins on next page)

28 November 2026

hydrogen

MDPI

Review

Degradation of Anion Exchange Membrane Water Electrolyzers Under Shutdown and Open-Circuit Transients: Protocols, Mechanisms, Diagnostics, and Mitigation

Md Mizanur Rahman * and Massimo Santarelli

Department of Energy (DENERG), Politecnico di Torino, Corso Duca Degli Abruzzi 24, 10129 Torino, Italy; massimo.santarelli@polito.it

* Correspondence: md.rahman@polito.it

Abstract

Anion exchange membrane water electrolyzers (AEMELs) are attractive for direct coupling to variable renewable supply, but their durability under the resulting transients is poorly constrained. This review examines AEMEL degradation under the intermittent test protocols reported at cell and stack level, focusing on the shutdown and open-circuit portions of those protocols. We classify the protocols by the electrical route through which the stop is imposed and set out what each reproduces of renewable-driven operation and what it does not. Reported degradation figures are re-expressed on a common per-cycle basis so that studies using different metrics, current densities and cycle counts can be compared. Three recurring losses emerge: oxidation and dissolution of non-noble hydrogen-evolution catalysts, ohmic drift of the membrane and ionomer after dry stops, and structural reorganization of the electrode under repeated reverse current. In the single cells resolved so far, open-circuit and reverse-current stops load the cathode, with a loss that scales with the cathode metal's stability; severity is set by the boundary conditions at the stop rather than by intermittency as such. Diagnostics and mitigation are assessed on that basis. The evidence base remains small, dominated by single cells, and rarely electrode-resolved, with one anode chemistry tested.

Keywords: anion exchange membrane water electrolysis; green hydrogen; intermittent operation; start–stop cycling; degradation; reverse current; open-circuit hold; shutdown transients

Academic Editor: Jan Janczak

Received: 13 October 2026
Revised: 2 November 2026
Accepted: 12 November 2026
Published: 18 November 2026

Copyright: © 2026 by the authors. Licensee MDPI, Basel, Switzerland. This article is an open access article distributed under the terms and conditions of the Creative Commons Attribution (CC BY) license.

1. Introduction

Currently, hydrogen production is dominated (~95% of global hydrogen) by methane reforming and coal-based routes [1]; less than 1% of the 2024 total came from renewable electricity [2,3], limiting climate benefits unless emissions are captured or displaced by renewable-powered electrolysis [3,4]. Electrolysis turns variable photovoltaic (PV) and wind output into a fuel that can be stored and drawn on when generation falls, and the IEA projects that couple electrolyzers to renewables could cut capital cost by ~30% by 2030 [3].

Under intermittent power, an electrolyzer is never subject to a stable DC load. It instead experiences irregular ramps, long periods at part load, pseudo-open-circuit

voltage states, and repeated off-load events. Martinez-Lopez et al. noted that renewable operation unfolds on more than one timescale [5]. Current and voltage follow the source almost immediately, whereas the thermodynamic and balance-of-plant variables behind them, temperature and pressure above all, move over minutes to hours, and it is often these slower variables that shape overall performance. These multi-timescale mismatches between electrochemical forcing and thermal–mechanical states can accumulate as stress in the cell; in liquid alkaline electrolysis, variable operation with simulated shutdowns has been shown to alter the crystal structure, composition and dissolution rate of Ni-based catalyst films [6].

Fluctuating renewable supply brings a distinct stressor: termination of operation caused by insufficient energy input. Studies frequently mimic this idle condition by applying off-load periods in the laboratory. This shutdown is defined by the boundary conditions imposed during the stop: electrical termination (true OCV, discharge path), hydraulic state (flow on/off, electrolyte connectivity), gas management (pressure differentials, crossover, purge/vent), and temperature evolution [7,8]. These boundary conditions govern whether the cell experiences only voltage collapse and relaxation or more aggressive stressors: catalyst redox transitions and element leaching [9,10], and reverse current, mixed-potential excursions and dissolution of both catalyst and support [6,11].

Quantitatively, the durability penalty of intermittent operation depends strongly on the imposed stop boundary condition. Under relatively stable operation, recent AEMEL single-cell studies reported degradation rates such as 84 $\mu V\ h^{-1}$ at 1 $A\ cm^{-2}$ over 1000 h [10], while long-duration AEM operation has also been reported at <1 $\mu V\ h^{-1}$ over 10,000 h [12]. However, shutdown-relevant stressors can generate much larger localized losses. For example, an imposed reverse current of −30 $mA\ cm^{-2}$ for 30 min caused ~55 mV cell degradation at 0.2 $A\ cm^{-2}$, with ~50 mV assigned to a PtRu/C cathode [13]. At stack level, shutdown protocol alone shifted degradation from 26 to 337 $\mu V\ cycle^{-1}$ depending on cooling and low-voltage dwell [8]. Intermittency is therefore not a single operating mode: the conditions imposed at the stop set its severity.

Among water electrolyzer technologies, the anion exchange membrane electrolyzer (AEMEL) combines features that are normally mutually exclusive. Its architecture is proton-exchange-membrane (PEM)-like—a polymer membrane separator and a compact MEA—while its chemistry is alkaline, which admits non-precious-metal (Ni, Co, Fe) catalysts. The result is a route to lower capital cost at high efficiency in a cell that still follows a dynamic load. AEMELs are vulnerable under renewable intermittency. Shutdown-induced reverse current (RC) degrades the electrode by dissolution and structural transformation, and recent work places it among the major failure pathways. Full reverse operation is not required: start-up transients on their own drive repeated redox cycling in the catalyst layers. In NiFe-based anodes, in-situ reconstruction toward NiOOH is accompanied by dissolution, agglomeration and collapse of the catalyst under fluctuating power, which accumulate as irreversible performance loss [14]. Intermittent duty profiles can produce reversible performance penalties (e.g., bubble accumulation and transient mass-transport blockage) alongside irreversible mechanisms, including OCV-time-associated catalyst dissolution, oxide formation, resistance increase and damaging cathode potential excursions [5,14]. Ursúa et al. reported that commercial electrolyzers are supplied with minimum load limits and lifetime-relevant caps on start–stop events, with one unit limited to ≤5000 start-up/stop cycles [15]. Beyond the cycle cap, degradation rates—typically expressed as voltage drift ($\mu V\ h^{-1}$) or efficiency loss per 1000 h [16]—directly determine stack replacement frequency and contribute a substantial fraction of the levelized cost of hydrogen (LCOH) [17,18].

Reviews of AEMEL electrolysis already cover steady-state materials and component durability well. Renewable-driven operation is the thinner part of that literature. What is missing is a synthesis connecting intermittent power profiles and the transient states they produce to degradation at the electrochemical, materials and stack levels, and connecting those causes in turn to mitigation strategies that can be checked in practice. That is the task taken up here. We also set out a preliminary severity vector for transient stressors: shutdowns, open-circuit holds, low-load periods and reverse-current events.

We argue that the durability challenge in renewable-coupled AEMEL has been framed too narrowly. The literature has concentrated on high steady-current operation and on cycling between high and low load. Reference-electrode-resolved diagnostics, post mortem analysis and controlled-protocol studies also point to shutdown transients and open-circuit and reverse-current excursions, a significant and underappreciated stressor class. In the single cells resolved so far, all with NiFe-LDH anodes, this stressor loads the cathode, most severely on non-PGM catalysts, and on PGM cathodes only under forced reversal. We bring those findings together and, having identified where diagnostic coverage fails, organize mitigation into a hierarchy across the operational, system and materials levels. The review is scoped to intermittent duty: steady-state chemical degradation of membranes and ionomers, catalyst design, and life-cycle assessment are covered in dedicated reviews [19–25] and appear here only where they bear on transient operation. Sections 2 and 3 summarize the context and define the intermittent test protocols used in the literature. Section 4 covers the diagnostic tools, electrochemical and operando/post mortem alike. Section 5 gathers the degradation evidence from these protocols and separates what every shutdown does from what a given protocol adds. Section 6 consolidates mitigation strategies at the operational, system and materials levels. Section 7 sets out the remaining knowledge gaps, and Section 8 concludes. Figure 1 provides a schematic overview of these linkages, mapping renewable stressor classes to their primary degradation mechanisms (Section 5), the diagnostic approaches that resolve them (Section 4) and the mitigation strategies (Section 6); it can serve as a navigation reference throughout the review.

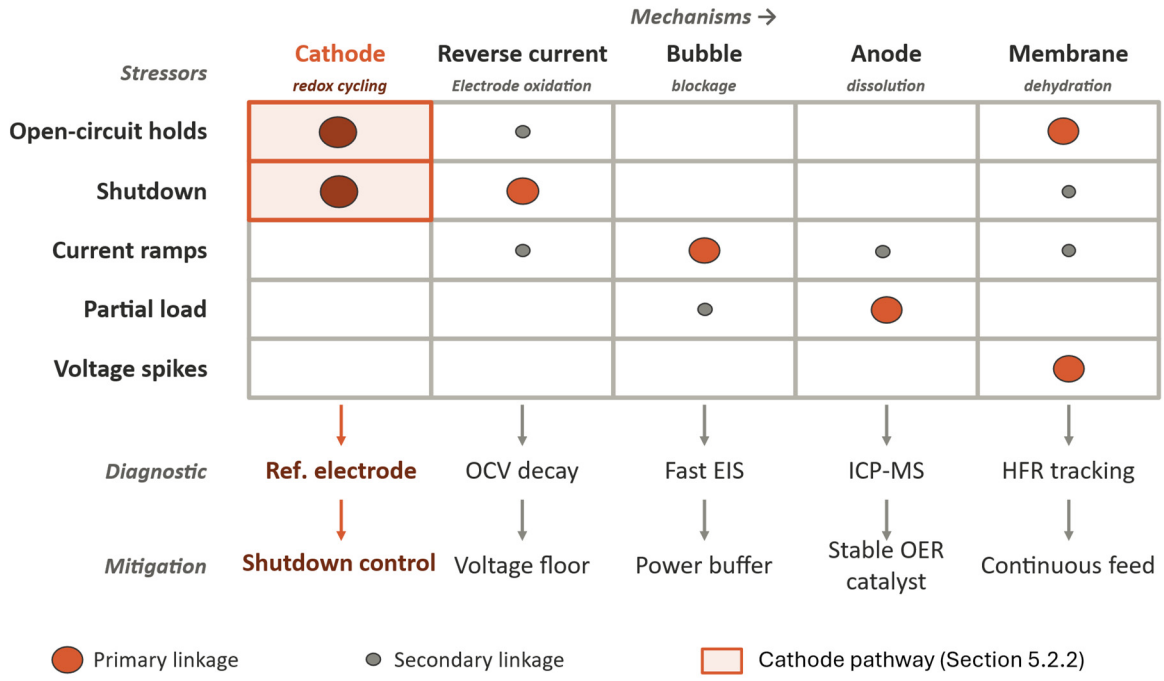


Figure 1. Linkage matrix relating renewable stressors to AEMEL degradation mechanisms, with the diagnostic and mitigation pairings discussed in Sections 4 and 6. Large markers denote a linkage

reported as dominant in at least one AEMEL study, small markers a secondary or AEL-derived linkage. Sources: open-circuit holds and shutdown–cathode [9,11,13]; shutdown–reverse current [6,8]; open-circuit holds–membrane [26,27]; current ramps [7]; partial load [14]; voltage spikes–membrane [12,28]. Highlighted cells mark the cathode pathway under open-circuit and reverse-current stops, resolved in single cells with NiFe-LDH anodes (Section 5.2.2).

2. Background and Context of AEMEL Technology

2.1. Hydrogen and the Integration of Electrolysis with Variable Renewables

Hydrogen is an energy carrier rather than a primary source: it stores energy from variable renewables, travels across sectors, and emits only water on use [19,20,29]. Water electrolysis is a central route from variable renewable generation to deep decarbonization [21,30], but deployment lags ambition: global installed water electrolysis capacity reached only ~2 GW by end-2024, with up to ~3 GW more expected to come online in 2025 [3].

Among variable renewable energy (VRE) sources, solar and wind account for more than 55% of large-scale electrolyzer projects worldwide [5]. Integration takes three forms: grid-connected electrolyzers, direct coupling to PV or wind, and hybrid architectures with buffering. In the grid-connected case, the cell receives a controllable load setpoint from grid-side power-system management. Direct coupling instead exposes the electrolyzer to rapid ramps, partial load, minimum operating limits and frequent on/off transitions.

An energy-balance study found that an electrolyzer coupled to PV or wind converted only 60% of the available renewable energy to hydrogen, and that frequent drops of wind power below the cell's minimum operating threshold produced 1.8-fold higher energy losses for wind than for PV [31]. A hybrid strategy—a 10 min minimum operating-time limit, a battery bank, or both—reduced start–stop events by up to 62.1% (PV) and 63.1% (wind), improving service life and raising overall efficiency by over 6% [15]. Power electronics govern how smoothly that load is delivered, since converter topology and ramp shaping set the current and voltage profile applied to the stack under fluctuating generation [32]. At system scale, electrolysis also supports sector coupling through power-to-hydrogen and downstream power-to-X (PtX) routes, acting as a controllable load and storage pathway for high-renewable grids [33].

2.2. AEMEL Technology and Its Position Relative to PEMEL and AEL

Interest in coupling water electrolysis to variable renewable supply has grown sharply since 2022. Figure 2a summarizes the publication record since 2015 and indicates that AEL and PEMEL dominate the volume while AEMEL is accelerating quickly in 2024–2025, indicating that renewable-coupled operation has become a mainstream research focus. AEMEL replaces the liquid electrolyte of conventional AEL with a thin solid AEM in a zero-gap MEA, thereby shortening the ionic transport path and enabling more compact designs [34–37]. The coupling of half-reactions results in the overall water-splitting process; associated reactions and respective potentials are shown in Figure 2b. Against this backdrop, AEMEL occupies an intermediate position between the two established technologies. It keeps the alkaline chemistry that lets AEL run on non-PGM Ni- and NiFe-based catalysts, while the thin solid membrane and zero-gap architecture deliver the compactness, current density and differential-pressure capability previously available only from PEMEL [34,38]. The trade-off is maturity: AEL is fully commercial and PEMEL is commercially established, whereas AEMEL remains at the R&D to early commercial stage and reported cell lifetimes are correspondingly shorter [38,39]. A second distinction, specific to AEMEL and consequential for standby strategy, concerns the feed. AEL requires concentrated KOH and PEMEL requires deionized water, whereas AEMEL can be operated on pure water, on dilute KOH up to about 1 M, or on dilute carbonate

[1,24,30,40]. The two feed modes are not at equal maturity: electrolyte-fed operation is the more developed, and the longest reported AEMEL durability test, ~12,000 h at 1.0 A cm^{-2}, was run under dilute KOH, whereas pure-water-fed operation has reached ~2200 h [1]. For intermittent duty, this positioning is decisive: PEMEL follows load transients readily, AEL is limited by slow start–stop and crossover at low load, and AEMEL is promising but still under active development [39,41]. Table 1 compares the three technologies on the attributes bearing on intermittent duty.

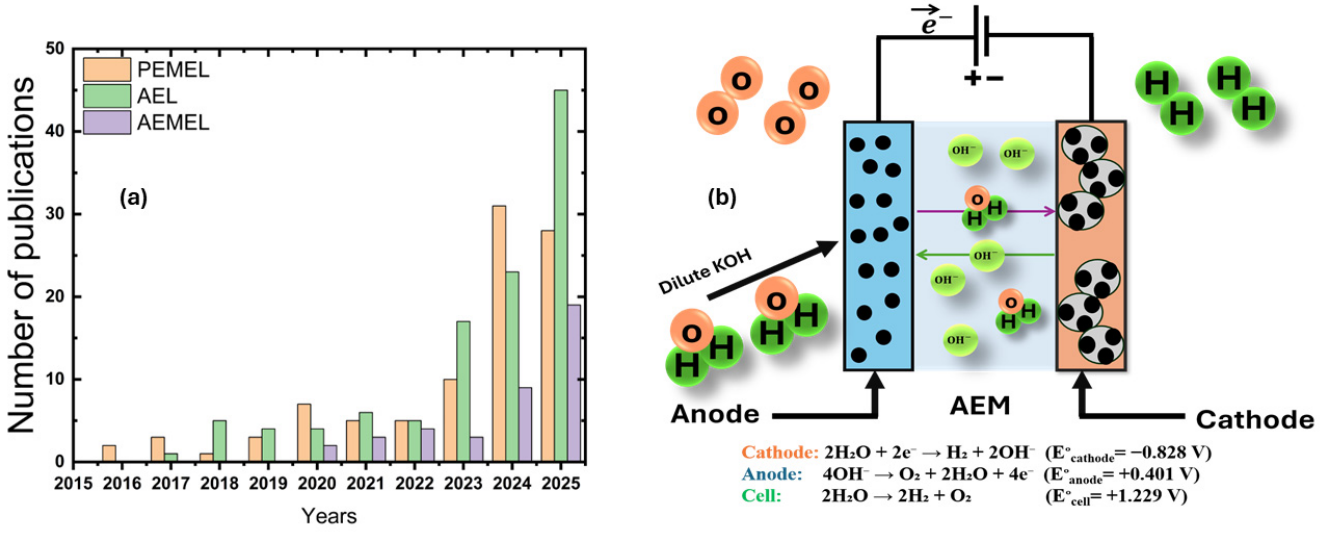


Figure 2. (**a**) Number of papers published in the last 10 years on electrolyzer coupling with renewable energy; (**b**) schematic of the three-layer MEA of an AEMEL cell and the function of each layer during electrolysis. Panel (**a**) compiled from Web of Science.

Table 1. Comparison of the principal characteristics of alkaline (AEL), proton-exchange-membrane (PEMEL) and anion-exchange-membrane (AEMEL) water electrolysis.

Attribute	AEL	PEMEL	AEMEL
Electrolyte/ion conducted	30–40 wt % (≈4.5–8 M) KOH; conducts OH^- [34,38,42]	Deionized (pure) water; conducts H^+ [35]	Pure water, dilute KOH (up to ~1 M) or 1 wt % K_2CO_3; conducts OH^- [34,38,39]
Separator/membrane (type, thickness)	Porous diaphragm (e.g., Zirfon Perl), ~500 µm [34,38,42]	Proton-exchange membrane (e.g., Nafion 115/117), ~50–200 µm [22,42]	Anion-exchange membrane (e.g., Sustainion, PiperION, FAA-3-50), ~20–100 µm [22,37]
Catalyst class (anode/cathode)	OER: Non-PGM (Ni, Ni–Co alloys) [34,38]; HER: Non-PGM (Ni–Mo-based alloys) [38]	OER: PGM (IrO_2, RuO_x) [34,37,38]; HER: PGM (Pt/C, Pt) [22,34,38]	OER: Non-PGM ($NiFeO_x$, Co_3O_4, TM oxides); optionally PGM (IrO_2) [22,34,38]; HER: Non-PGM (Ni-based, TM); optionally PGM (Pt/C) [34,38,39]
Typical current density	0.2–0.8 A cm^{-2} [34,37,38]	1–3 A cm^{-2} [34,38]	1–2 A cm^{-2} [34,38]
Operating/differential-pressure capability	Pressurized feasible (1–30 bar); limited differential-pressure tolerance (crossover via diaphragm) [38,39]	High differential-pressure capability (typ. 15–30 bar) [22,37–39]	Electrochemical H_2 compression up to ~30 bar; differential pressure demonstrated at ~7 bar (100 psi) [1,34]
Dynamic/intermittent-operation suitability	Limited; slow start–stop, sensitive to crossover at low load [38,39]	Excellent; rapid load-following dynamics [34,38,41]	Promising; under active R&D for intermittent renewable coupling [39,41]

Technology readiness/maturity	Mature/fully commercial [22,38]	Commercial (esp. small–medium scale) [38]	Emerging/R&D to early commercial [38,39]
Reported durability/lifetime	~60,000–100,000 h stack lifetime [38,41]	~20,000–60,000 h (60,000+ h projected) [34,42]	~12,000 h at 1.0 A cm^{-2}, 60 °C, 1 M KOH (0.7 μV h^{-1}); ~2200 h pure-water-fed at 0.2 A cm^{-2}, 50 °C (0.2 mV h^{-1}) [22,34,42]

3. Challenges Under Intermittent Power Input

3.1. The Nature of Renewable Intermittency

The fluctuation imposed on a directly coupled electrolyzer is set by the weather rather than by the operator, so it is neither scheduled nor bounded in advance. When electrolyzers are coupled directly to these sources off-grid, they accept whatever current or voltage profile the source delivers in place of a steady load [15,43,44]. Figure 3a shows the resulting intermittency under three weather conditions: a clear-sky day, a partly cloudy day and a broken-cloud day. Figure 3b shows a stochastic wind-derived profile.

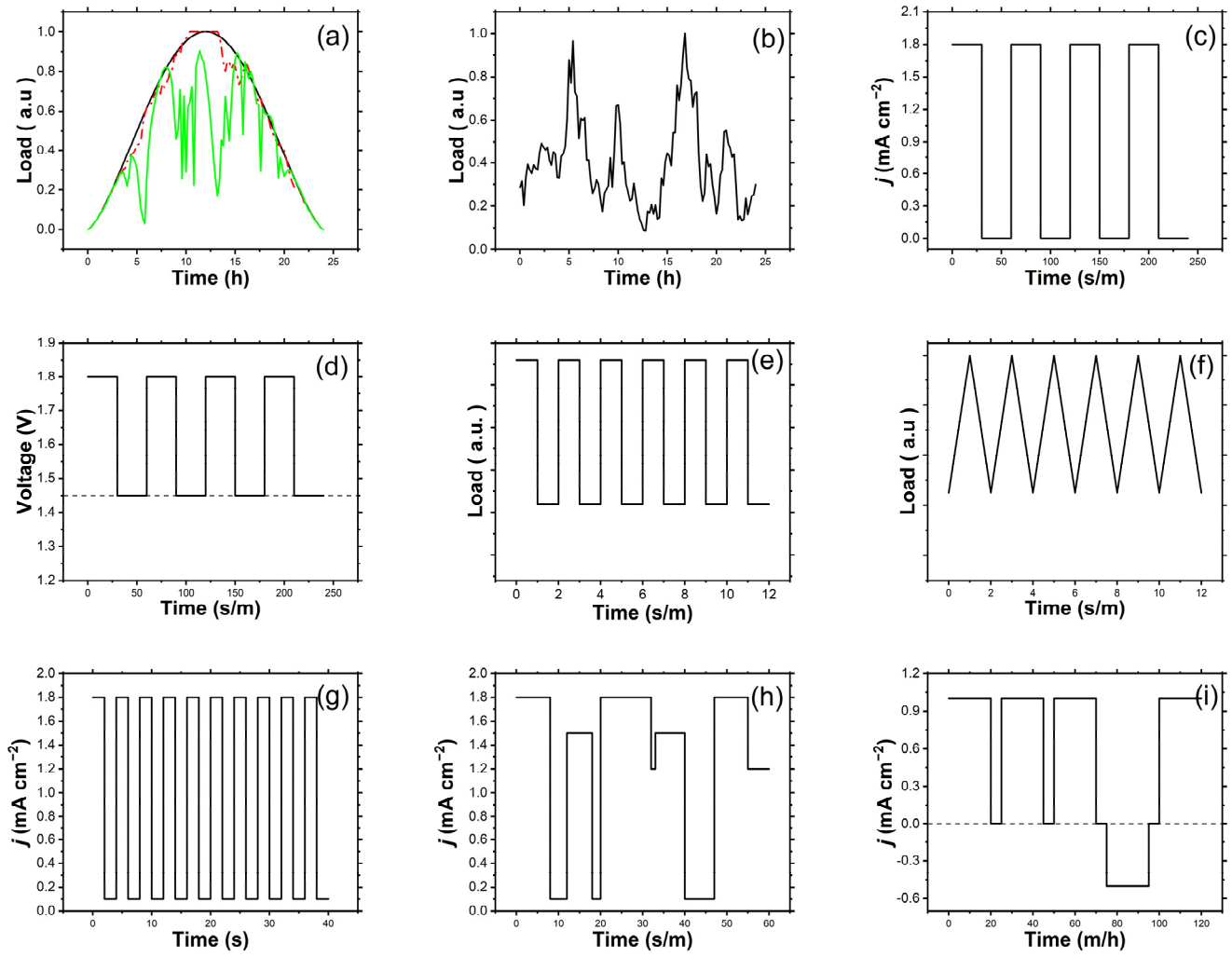


Figure 3. Representative input and load profiles used in intermittent-operation studies. (**a**) Solar PV output over a 24 h day for a clear sky (black), a partly cloudy day (red, dash-dot) and a broken-cloud day with short-term fluctuations (green); (**b**) stochastic wind-derived profile; (**c**) start–stop cycling between full load and zero load; (**d**) start-pseudo-OCV cycling between 1.8 V and a 1.45 V lower bound; (**e**) square-wave cycling; (**f**) triangular-wave cycling; (**g**) pulse-based cycling with a

short step size; (**h**) irregular cycling with varying step size and amplitude; (**i**) forced polarity inversion, with the dashed line marking zero current.

Cloud transients, diurnal cycles for PV, and wind gusts for wind turbines set the time scale of intermittency in the renewable profile, which spans seconds to hours. Electrolyzers must therefore accommodate both high ramp rates and deep excursions in load [45]. A test profile representative of genuine renewable events must reproduce these rapid, deep, partial-load excursions rather than switch between zero and full current in the laboratory [14]. Such realistic current or voltage profiles generate complex voltage histories, with frequent partial-load holds, near-idle or open-circuit voltage holds, and sharp on–off transitions that stress both the cell components and the balance of plant (BoP) [43].

3.2. Laboratory Protocols Used to Emulate Intermittent Operation

Recent studies use various intermittent test protocols at laboratory scale; details are listed in Table 2, and the profiles fall into four categories. The first category comprises square- and triangular-wave current or voltage cycling profiles [14,28,46], in which the cell is cycled between a high and a low—but not zero—current at fixed intervals; representative examples are shown in Figure 3e,f. Alternating or ramping the cell voltage instead of the current is also a common strategy [14,28,47].

Table 2. Intermittent test protocols applied to AEMEL in recent laboratory studies. Protocols from liquid alkaline studies are listed in Table S1.

Technology	Cell Type	Protocol Class	Protocol Specifications
AEMEL	Single cell	Square wave cycling	2.0 ↔ 0.1 V cycling, 2 min cycle time, 1000 cycles [28]
AEMEL	Single cell	Pulse based intermittent profile	2.4 ↔ 0.02 A cm^{-2} cycling, 4 s cycle time, 11,000 cycles [12]
AEMEL	Single cell	Stepwise cycling with low-bias hold	2.0 ↔ 0.5 ↔ 0.005 A cm^{-2} (near-OCV) steps, 10 min each, 10 h, 110 °C; preceding a 500 h hold at 1 A cm^{-2} [51]
AEMEL	Single cell	Square and triangular waves	2/1.45 V square vs. triangular waves [46]
AEMEL	Stack (19 cell, 60 cm^2/cell)	Cold start, start–stop cycling	Voltage ramp 1.23→1.8–2.1 V in 12–240 s; 10 min load; complete shutdown; varying stop time (0 to 4 h) [7]
AEMEL	Single cell (flow)	Reverse-current/polarity inversion	Polarity reversal giving 0.03 A cm^{-2} reverse current for 30 min [13]
AEMEL	Single cell	Square wave cycling, wind profile, and rest period.	1.50/1.70 V square waves; Cycled time: 400 s,1000 s,3000 s; Wind profile: fluctuate between 1.2 and 1.8 V for 80 groups, including a 100 h rest after 40 groups [14]
AEL + AEMEL	Single cell	Start–stop cycling	0.5 A cm^{-2} 7-min on/7-min off, 0.05 A cm^{-2} s^{-1} ramp-down rate, 14 min cycle time, 360 cycles [48]
AEMEL	Single cell	Start–stop cycling	1 A cm^{-2} 30 min on/OCV 30 min off, 60 min cycle time, up to 192 cycles [9]
AEMEL	Stack (22 cell, 60 cm^2/cell)	Start–stop cycling	0.85 A cm^{-2} 30 min, then internal/external discharge to 0–1.2 V for 20–40 min, with/without cooling [8]
AEMEL	8-cell stack, 512 cm^2, 2.5 kW	Simulated solar cycling with start–stop	13 simulated solar cycles, >50 h total, 1 A cm^{-2} peak at 1.78 V per cell, 60 °C; repeated start–stop and load fluctuation [52]
AEMEL	Single cell	Square waves cycling	0.10↔1.60/1.80 V square waves, 2 min cycle time, 150 cycles [47]
AEMEL	Single cell	Start–stop with partly square-wave, polarity inversion	Start–stop with step: OCV (1 min) ↔ 0.1 A cm^{-2} (1 min) ↔ 1.0 A cm^{-2} (1 min) for 50 h (1000 cycle); Start–stop: OCV (1 h) ↔ 1 A cm^{-2} (1 h), 50 h; reverse -current (RC) by polarity inversion protocol: −30 mA cm^{-2} for 30 min [11]
AEMEL	Single cell	Start–stop cycling	5 h at 500 mA cm^{-2} + 12 h OCV, continuous 1 M KOH feed [50]

AEMEL	Single cell (5 and 100 cm^2)	Steady CC with interruption, square wave	1 A cm^{-2} CC (2000 h) with routine stop to electrochemical diagnostic; 0.2↔1 A cm^{-2} cycles [53]
AEMEL	Single cell	Start–stop cycling	Protocol A: repeats between 1.95 V (2–10 h)/OCV-stop (12 h) for 1000 h. Protocol B: Repeats 1.95 V (100 h)/OCV-stop (12 h) for 1000 h. No KOH feeding during OCV periods [27]

The second category is start–stop, in which the cell alternates between a high current and a complete stop at zero load; resting times range from minutes to hours [7,48]. It is also called on/off or startup/shutdown [49], and start/OCV–stop, since the cell rests at open-circuit voltage. Figure 3c shows a typical start–stop profile. Nam et al. [11] investigated the relative durability of Pt-based alloy catalysts (PtNi/C, PtCo/C, PtRu/C and Pt/C) under a mixed start–stop protocol they termed the intermittent protocol, pairing a stepwise cycle through OCV and two current densities with a longer OCV/high-current cycle of equivalent total duration. Niaz et al. examined the effect of open-circuit holds under KOH on/off operation [26,27,50].

The third category, pseudo-OCV, is a special square-wave cycling scheme in which the applied load switches from a high load to a low bias current—shown schematically in Figure 3d—holding the cell near its open-circuit voltage. Because the voltage does not fall to zero, the cell avoids exposure to a reverse-current (RC) event and the associated degradation. A single-cell AEMEL study used 1.45 V as the low level [46]..

The fourth category, the pulse-based intermittent profile, alternates current or voltage with a very short step size. Motealleh et al. [12] reported 2 s at a high current density and 2 s at a low one over 11,000 cycles. Because the ramp up and down is instantaneous, the cell experiences a repetitive voltage shock. Figure 3g shows a protocol with a short step size.

The protocols above impose shutdown through distinct electrical routes, which are not interchangeable stressors even when reported under one heading. Five regimes can be separated. (i) In a low-load or pseudo-OCV hold the cell remains under a non-zero bias, so both electrode potentials stay within their operating polarization window and no reverse-current event occurs. (ii) In a passive true-OCV hold, the load is removed with no external discharge path, and the cell voltage falls first through the instantaneous ohmic drop and then through a redox-controlled relaxation (Figure 4a). (iii) Internal self-discharge is the reverse current that this relaxation drives through the ionic path remaining between the electrodes, sustained by charge stored in the double layers and in surface redox states and by gas retained in the porous structures (Figure 4b). (iv) Controlled external discharge imposes an additional external path that clamps the cell voltage and draws the same stored charge at a higher rate. (v) Forced polarity inversion applies an externally sourced negative current that drives the cathode anodically beyond the potential reached by self-discharge alone.

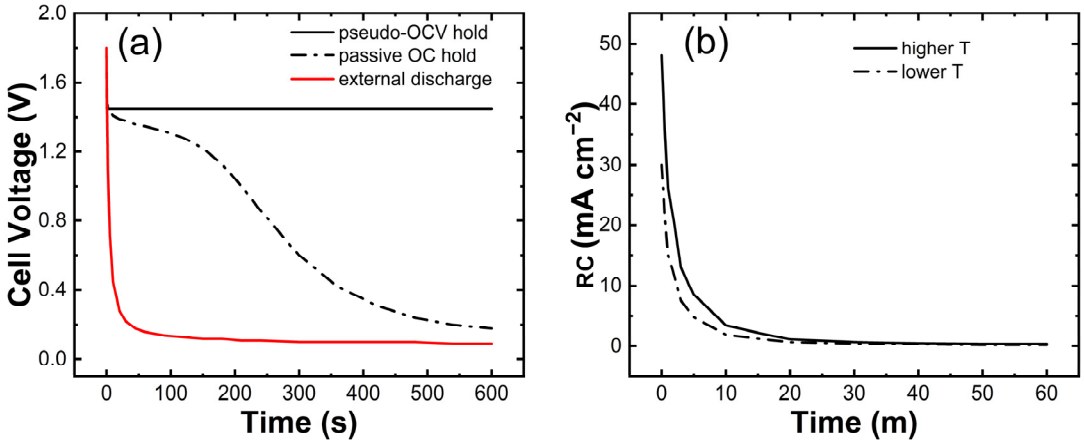


Figure 4. Schematic cell response after load removal, for the discharge routes defined in Section 3.2. (**a**) Cell voltage, showing the instantaneous ohmic drop, the redox-controlled plateau and the subsequent relaxation. (**b**) Magnitude of the internal reverse current density following a passive shutdown, at two operating temperatures. The curves are schematic; absolute values are not taken from measurement.

Severity does not increase monotonically along this sequence. Internal and controlled external discharge differ mainly in rate: in the one stack where both were compared, the route changed how fast the stack discharged but not the per-cycle drift, which depended instead on how long the stack was then held at 0 V at operating temperature (Section 5.2.3) [8].. Forced polarity inversion is not a shutdown route: the reverse current is supplied from outside the cell, and the protocol is used as an accelerated stress test representing a worst case rather than an operating state. Results obtained under forced inversion are therefore reported here as an upper bound on shutdown severity, and are identified separately from passive open-circuit evidence throughout.

Two terms are used consistently in what follows. A shutdown transient is the dynamic event that begins when load is removed and ends when the cell settles at a stable low voltage; its course, the reverse current and the rate of voltage decay, is set by the discharge route, that is by regimes (ii) to (v) above. An open-circuit hold is the period the cell then spends in that state, and its severity is set by duration, temperature and electrolyte condition. The two are separable stressors with different controlling variables and are reported separately throughout.

Mixed protocol types are commonly used in laboratory testing, with variation in on-load and stop-load magnitude and duration, in ramp rate, and in waveform making the operation more complex but closer to real-world cycling. Figure 3h shows an irregular protocol with a varying step size. Rahman [54] mimicked a wind turbine power profile to design a wind profile suitable for single-cell PEMEL degradation testing, including ramp rates from ultra-low to very high, OCV stops, pseudo-OCV stops, and square and triangular waves. Gladik et al. [7] varied the ramp-up time (12, 120 and 240 s) and target voltage of cold starts in a stack to trace their effect on degradation over repeated start–stop cycles, and showed separately that longer downtimes before a restart (0 to 4 h) widen the cell-to-cell voltage spread on restart, with overshoots of ~400 mV after 4 h. Wan et al. [14] applied a wind-derived voltage profile for 80 groups, with a 100 h rest period after 40 groups while maintaining the water supply.

Intermittent test protocols are often designed to target degradation in a specific cell component. To study chemical and mechanical degradation of the membrane and the catalyst, open-circuit holds and pseudo-OCV holds are frequently used. Guruprasad et al. [13] reversed the polarity of the electrodes, applying a negative current of 0.03 A cm^{-2} for

30 min to probe the worst case that could arise from reverse current during open-circuit holds; the same protocol was also used by Nam et al. [11].

Intermittent test protocols that include a shutdown step are common stressors for both AEL and AEMEL technologies. AEL profiles, however, generally operate at the stack or system level (multi-cell, with manifolds and circulation on or off), because the liquid-electrolyte pathway and the bipolar design make reverse-current and shutdown behavior strongly dependent on electrolyte circulation [8,13,55]. In AEMEL, intermittent test protocols are more often imposed at the cell or MEA level, so ionic-pathway and low-concentration electrolyte management are the main controlled strategies during shutdown [26,27,50,53].

Using intermittency in a three-electrode configuration is a widely used approach for materials studies in alkaline water electrolysis (AEL) and for mechanistic studies relevant to AEMEL components. These profiles are straightforward to model and are designed as programmable stepwise waveforms rather than as imitations of realistic energy sources [6,43,48]. The three-electrode system (working, counter and reference) decouples the anode and cathode potentials in the first transient. Repeated load steps, start–stops, charge–discharge polarity inversion and start-OCP rests are therefore generally used to locate the intermittent stressor. Marquez et al. [6] conducted a comprehensive study under different protocols, covering OCP decay, three-electrode stability, on/off operation without forced RC, and intermittent operation with imposed RC. To track both fast and slow discharge behavior, the authors used chronopotentiometry (CP) steps of 480 s and 10 s with OCP rests of 30 s and 1 h. The hour-long OCP exposure reveals the rate at which Ni-based hydroxide and oxyhydroxide films relax through their redox transitions [6]. Oda et al. [56] modeled a charge–discharge RC profile.

Of the studies collected in Table 2, only one applied a profile derived from measured generation: a wind-power record scaled to a 1.2 to 1.8 V envelope [14]. The remainder are synthetic waveforms, and four limitations follow from that. They impose a regular period where real generation is stochastic, so effects depending on the distribution of event intervals cannot appear. They vary current or voltage alone while temperature, pressure and flow are held constant, whereas in a real system these co-vary on the slower timescales noted in Section 1. They compress damage into cycle counts far below a service lifetime. And they are overwhelmingly single-cell, omitting the manifold and shunt pathways that govern stack behavior. The evidence reviewed here therefore establishes mechanism and ranks severity between protocols but does not support absolute lifetime prediction under field conditions.

3.3. Discharge Timescales During a Stop

During a stop the cell or stack discharges and the electrode potentials rebalance, so the duration of the stop sets how far and how fast these processes run; stop duration is therefore a primary design variable in realistic profile studies [7,8]. The characteristic timescale differs between PEMEL, AEMEL and AEL because the ionic path length between the electrodes and the gas and electrolyte inventory of the flow structures differ.

Traditional AEL bipolar stacks are built with long, complex electrolyte transport pathways known as manifolds, which keep the cells ionically connected after the load is removed. Reverse current driven by electrode-potential drift can therefore persist for tens of minutes to hours, and the discharge rate depends strongly on the gases retained within the manifolds and the electrolyte channels. Abdel Haleem et al. [55] noted that ~30 s is required for bubble evacuation to reach the RC maximum, after which an ionic RC can persist for ~5000 s before it decays. Only the electrically isolated end-plate electrodes kept their potentials apart over the ~10,000 s (2.7 h) record; on the bipolar plates, the reverse

current drove the anode potential down and the cathode potential up, exposing the anodes to reduction and the cathodes to oxidation [55].

By contrast, a zero-gap AEMEL cell has an ionic path of only tens of micrometers and no shared manifold, so the discharge is confined to the cell itself; what continues during the hold are slower electrode changes, such as the spontaneous oxidation of a metallic Ni cathode toward α-$Ni(OH)_2$ under open circuit, which proceeds over minutes to hours [9]. At stack level the same technology behaves differently: an AEMEL stack shows an OCV plateau that collapses within ~49 min with electrolyte circulation and ~378 min without it, so the timescale is set by cell architecture and BoP rather than by the technology label [8]. Because real transients range from ultra-short to hours-long, many AEMEL studies concentrate on short, repeatable on–off stressors: 30 min reverse polarization is used to mimic a severe shutdown [13], and on-load durations of 10, 30 and 60 min are compared to resolve the effect of cycling frequency in the intermittent test protocol [8]. Some tests use a long start-OCV hold, for example 5 h on at 500 mA cm^{-2} followed by 12 h OCV, which represents a different timescale regime from fast on/off cycling.

Most of the mechanistic evidence on shutdown and reverse current was obtained in liquid alkaline electrolysis, not in AEMEL. Transfer has to be licensed rather than assumed, and four properties decide whether a given result carries across: the ionic path length between the electrodes, the concentration, conductivity and inventory of the electrolyte, the redox-active surface inventory per unit membrane area, and the shunt pathways through manifolds and bipolar hardware. A mechanism resting on electrode surface chemistry alone transfers reasonably, since that chemistry is shared. Ni oxyhydroxide reduces to the hydroxide and toward a more metallic state under deep discharge in either system; Ni and Mo are unstable at open-circuit potential in either; the damaging potential windows are the same, and so is the principle behind sacrificial cathodic protection. Architecture-dependent mechanisms transfer less readily. Absolute discharge timescales, the magnitude of manifold-driven reverse current and how it distributes across the cells of a bipolar stack, the sensitivity of that current to electrolyte circulation, and the contribution of macroscopic retained gas all follow from a liquid inventory and a flow geometry that a zero-gap MEA does not have. AEMEL runs below 1 M against 6–7 M in AEL, and its ionic path is tens of micrometers rather than a manifold. Results from liquid alkaline systems are therefore identified as such in the sections that follow, and are used to establish mechanism rather than magnitude.

4. Diagnostics and Evaluation Methods

4.1. Diagnostic Goal Under Intermittent Operation

A single end-of-test polarization curve cannot identify the origin of a loss. Practice under intermittent test protocols has moved toward time-resolved evaluation built for attribution. The first aim is to distinguish reversible from irreversible loss, the second to resolve the remainder into ohmic, kinetic and mass-transport contributions, and the third to localize degradation at the anode or the cathode.

Table 3 summarizes the techniques reviewed below: what each resolves, when it can be acquired relative to a stop, its main limitation and the AEMEL studies that have used it. The subsections set out why each measurement works and what it cannot attribute.

Table 3. Diagnostic techniques used under intermittent and shutdown protocols, with what each resolves, when it is acquired relative to a stop, its main limitation, and the studies that have applied it. AEL denotes liquid alkaline studies.

Technique	What it Resolves	When Acquired	Main Limitation	Applied in
OCV/OCP decay tracking	Internal discharge, reverse current, redox plateaus	During the stop	A plateau cannot be assigned to a redox couple from the voltage trace alone	Gladik et al. [8]; Nam et al. [11]; Marquez et al. (AEL) [6]; Abdel Haleem et al. (AEL) [55].
Fast (truncated) EIS	High-frequency resistance: hydration, contact resistance; continuous iR correction	During transients and short rests	No low-frequency information; cannot be used for DRT	Koch et al., [57].
Gas crossover sensing	H_2 in O_2 at the anode outlet; crossover current	During operation and stops	Not yet logged continuously through a shutdown and restart	Gladik et al., [7]; Motealleh et al., [12].
Reference electrode	Separate anode and cathode potentials	During and after the stop	Single cells only; pseudo-RHE unreliable above 0.2 A cm^{-2}; sensitive to electrode misalignment	Jeon et al., [9]; Guruprasad et al., [13]; Nam et al., [11]; Mar et al., [58].
Offline ICP-OES/ICP-MS	Cumulative dissolved metal per element	End of test	Cannot time dissolution to a stressor within the protocol	Wan et al., [14]; Guruprasad et al., [13].
Online ICP-MS	Time-resolved dissolution, including bursts on reoxidation	During the protocol	Shown so far only in a half-cell flow cell	Marquez et al., (AEL) [6].
Operando Raman/SERS	Phase changes (NiOOH ↔ $Ni(OH)_2$) during discharge and restart	During the protocol	Requires an optical cell; not yet applied inside an operating MEA during a stop	Marquez et al., (AEL) [6].
SEM, FESEM, FIB, TEM, EDX	Thinning, cracking, detachment, agglomeration, element loss	Post mortem	End point only; assembly and disassembly can add artefacts	Galkina et al., [10]; Wan et al., [14]; Niaz et al., [27].
ToF-SIMS, XRD, XPS	Depth-resolved composition; bulk phase; surface oxidation state	Post mortem (BOT and EOT)	XRD misses surface phases; XPS samples only the top nanometers	Marquez et al., (AEL) [6]; Jeon et al., [9]; Nam et al., [11].
Polarization curve (iR-corrected)	Overall loss; ohmic versus kinetic split	Checkpoints	Aggregates both electrodes; reversible and irreversible loss mixed unless a rest is inserted	Galkina et al., [10]; Shaik et al., [47]; Wan et al., [14].
Full-spectrum EIS and DRT	Ohmic, kinetic and transport contributions; separated processes	Checkpoints at steady state	Needs a stable steady state; peak assignment rests on few AEMEL studies	Ranz et al., [59,60]; Fang et al., [61]; Sampathkumar et al., [62].
Cyclic voltammetry	Double-layer capacitance, ECSA, redox features	Checkpoints, mostly three-electrode	Mostly half-cell (RDE) rather than full cell	Wan et al., [14]; Nam et al., [11]; Jeon et al., [9].

4.2. Time-Resolved Transient Capture: OCV Tracking and Fast EIS

The methods collected in this subsection are those that can be acquired during a transient, whereas full-spectrum impedance and the analyses derived from it require a stable steady state and are therefore applied at checkpoints on either side of the transient.

Open-circuit voltage (OCV) tracking during a stop: Tracking the cell voltage during a stop is the most direct diagnostic of start–stop operation. The shape of the decay reveals the internal discharge processes, the reverse current and the plateaus that indicate which electrochemical couples control the relaxation of the electrode potentials [8,55,63]. In AEMEL studies, open-circuit holds appear either as conditioning before performance testing [10] or as periodic holds within the intermittent profile [11], and decoupling the electrode potentials with a cathode-side reference electrode is emerging as the more

informative variant [9]. Plateau assignments should be supported by operando spectroscopy or post mortem surface chemistry rather than by the voltage trace alone [6].

Fast EIS: Full-spectrum EIS requires a stable steady state, which makes it poorly suited to shutdown, reverse current or fluctuating load. Fast EIS truncates the sweep to the high and mid frequencies, for example 500 kHz–1 kHz, to locate the high-frequency resistance quickly at each current step, so that membrane hydration and contact resistance can be followed as conditions change, such as under dry-cathode operation [57]; impedance recorded at each step of a stepwise polarization curve likewise supplies the high-frequency resistance for iR correction [42], isolating the kinetic overpotential at each electrode [9–11].

Gas crossover: Gas crossover matters for safety at low load and during stops, and has been followed with an anode-outlet thermal-conductivity sensor, which showed less than 1% H_2 in O_2 with the highest fraction at low current density [7], with an LSV limiting-current proxy [12] and by outlet gas chromatography.

4.3. Electrode-Resolved Attribution (Reference Electrodes)

Standard full-cell polarization and impedance measurements aggregate the anode and cathode contributions into a single response, obscuring which electrode drives the degradation observed under intermittent operation. A reference electrode removes that ambiguity, and three configurations have been used in recent AEMEL work. In the first, an extended membrane tongue carries the ionic connection to an external reversible hydrogen electrode (RHE) in a KOH-filled chamber, avoiding hardware in the catalyst layer [9,11]. Because the tongue extends orders of magnitude farther than the membrane is thick, the reference senses the potential at the membrane mid-plane; with this configuration, Tricker et al. showed that anode kinetics dominate the cell kinetic loss, whereas mass transport dominates the cathode overpotential under electrolyte feed [64]. In the second, a Pt wire contacts the membrane outside the active area and is biased with 20–30 μA to hold 0 V vs. RHE through local hydrogen coverage. Guruprasad et al. [13] placed it on the cathode side, because evolving O_2 shifts the local equilibrium near the anode. In the third, an edge-type Hg/HgO electrode reaches the membrane edge through an electrolyte bridge in the flow plate, which keeps the junction hydrated over stability tests exceeding 200 h [58]. Combined with distribution of relaxation times (Section 4.6), a dual reference arrangement decoupled the ohmic, kinetic and mass-transport overpotentials of each electrode in a 25 cm^2 cell over a 1000 h test [62]. Each configuration has a limitation. The tongue adds an ionic path that may carry its own iR drop and must stay hydrated; the Pt-wire pseudo-RHE depends on a stable bias current, and its potential drifts above 0.2 A cm^{-2} [13]. Electrode misalignment shifts the sensing point of an edge-type reference and makes half-cell impedance frequency-dependent, so Mar et al. [58] found three-electrode cyclic voltammetry more reliable than decoupled polarization curves or impedance for tracking electrode loss. None has been demonstrated at stack scale, where shunt currents and cell-to-cell imbalance complicate the potential reference.

4.4. Surface Chemistry and Dissolution: ICP-MS, ICP-OES, Raman and SERS

Shutdown and reverse-polarity stressors drive chemical transformation and dissolution, documented by ICP-OES and ICP-MS, operando Raman and SERS, and ToF-SIMS. Marquez et al. [6] provided the most complete dataset, pairing OCP diagnostics with operando spectroscopy, online ICP-MS at the outlet of a flow cell and depth profiling. Most AEMEL studies instead sample the electrolyte offline, usually at the end of the test: Wan et al. [14] found Ni dissolution more than 40-fold larger at a 200 s than at a 1500 s fluctuation interval, and Guruprasad et al. [13] measured a 36% Ru loss from PtRu/C and substantial Mo loss in the catholyte after polarity inversion. An end-point sample ranks

materials under identical cycling but cannot show when the dissolution occurred or which stressor caused it; an online measurement can.

Operando Raman and SERS capture phase reduction under reverse current and the incomplete reoxidation that follows. Using in situ SERS on Ni-based hydroxide films in alkaline electrolyte, Marquez et al. [6] showed that a stop at open-circuit potential returns the surface only to the hydroxide, whereas reverse-current steps drive a deep discharge toward a more metallic phase, after which the oxyhydroxide does not fully re-form on the next OER step, including for $NiFe(OH)_2$. Over longer durations, reconstruction is better mapped ex situ: in a NiFe-LDH anode operated at 1 A cm^{-2}, Galkina et al. [10] observed γ-NiOOH bands at 480 and 560 cm^{-1} emerging after 500 h, overlapping by 1000 h with γ-FeOOH bands near 526 and 690 cm^{-1} as the catalyst converted fully to Ni(Fe)OOH.

4.5. Post Mortem Structural Analysis: SEM, FIB, XRD and XPS

Post mortem analysis supplies the physical evidence that confirms or corrects the electrochemical diagnostics. Section 4.4 covered what leaves the electrode; these methods resolve what stays behind, namely the structure of the catalyst layer and its interfaces and the crystalline and near-surface states that repeated stops leave in it.

SEM, FESEM, TEM and EDX document catalyst-layer thinning, cracking, detachment, delamination and agglomeration, and FIB milling gives true cross-sections through the substrate, catalyst layer and membrane [10]. Cross-sections quantified the interval dependence of anode thinning under square-wave cycling (Section 5.2.1) [14]; SEM found the catalyst layers still attached to the membrane after ~1000 h of on–off operation, which led the authors to exclude the electrodes and interfaces as the source of the irreversible loss [27]; and FIB-SEM tracked agglomeration, cracking and selective Fe loss as operation lengthened [10]. In AEL, SEM showed severe coating cracks in RuO_2/Ni after reverse current [65].

ToF-SIMS adds depth-resolved chemistry: under reverse-current cycling, NiCo films thinned from ~110 to 40 nm and NiFe films from ~160 to 130 nm, with large losses of key elements [6]. XRD pairs at BOT and EOT identify phase changes such as β-$Ni(OH)_2$ formation [9] and partial Ni oxidation to NiO [66]; for Pt-based alloys, XRD confirmed the initial alloy structure, and its fate after testing was followed by TEM and XPS [11]. XPS quantifies the topmost nanometers, where oxidation, adsorbate accumulation and element redistribution appear first; it has been used to track Ni^{2+} and Ni^{3+} signatures [6,10,14,49], incorporated K and catalyst-element depletion [53], and, with Ar^+ sputtering, subsurface states masked by surface oxidation [9].

4.6. Standard Electrochemical Benchmarks: I–V, Full-Spectrum EIS and CV

I–V curves and iR-corrected performance: Polarization curves under start–stop operation are most useful as a comparative workflow, measured at periodic checkpoints, rather than as a single-point performance score taken at BOT and EOT. A realistic profile with an OCV stop can quickly alter the hydration state, the interfacial contact resistance, the charge state of the electrodes and the bubble-management conditions, so an observed voltage rise may reflect a reversible transient resistive or transport penalty rather than an irreversible contribution. Correcting the net performance loss for iR is therefore commonly used to separate the kinetic losses from the ohmic ones [47,48]. Across AEMEL studies, I–V performance is measured mostly by two techniques: (i) galvanostatic steps, that is, current steps with holds, and (ii) potentiostatic voltage sweeps (LSV) which are the more common of the two. Step-based polarization starts at a very small current (~0.016 to 0.02 A cm^{-2}) and runs up to 1.5 A cm^{-2}, in some cases extending to 2 A cm^{-2}, with a dwell time of 60 to 120 s at each step to let the reading stabilize [53]. LSV is reported over a range of 1.2 to 2.1 V at a scan rate of ~5 to 20 mV s^{-1} [26,50]. Many AEMEL studies do not

benchmark I–V continuously during start–stop or intermittent cycling, but instead measure BOT and EOT and sometimes routine checkpoints. For a long-duration durability test, I–V has been reported at every 100 h of a 1000 h test [10], after every 50 h of voltage cycling [14], and after every 24 intermittent cycles [9].

Impedance spectroscopy (EIS): In contrast to the truncated fast-EIS approach used for transient capture (Section 4.2), full-spectrum EIS at periodic checkpoints provides the complete ohmic, kinetic and transport decomposition needed to attribute steady-state degradation. In situ EIS allows degradation to be assigned to primarily ohmic contributions at the interfaces, the AEM and the contacts, to kinetic contributions at the electrode and the catalyst layer, or to transport-related contributions associated with bubble and electrolyte management. EIS is widely used across studies because it detects reversible effects such as bubble blockage, the resistance changes that develop regularly during intermittency, and the distinct changes triggered by shutdown and restart. The common EIS practice is a potentiostatic voltage hold, most often at 1.4 to 2.1 V, with an AC amplitude of 10 mV over a frequency range of 100 kHz to 100 mHz [14,53]. Another common pattern is galvanostatic EIS at a fixed current, for example 50 to 200 mA cm^{-2}, with a perturbation of 10 mV [9] or 10% of the applied current [13].

Distribution of relaxation times (DRT): DRT converts an impedance spectrum into a distribution over characteristic time, so that processes overlapping in the complex plane resolve into separate peaks, with the area under each peak corresponding to the resistance of the process behind it and without an equivalent circuit having to be chosen in advance [67]. Under intermittent duty the benefit is practical: one process can be followed between checkpoints while the others stay in view, which is what loss attribution across a start–stop or idle step requires. Peak assignment in AEMEL rests on a small number of studies, which agree on the ordering more than on the frequencies themselves, placing ionic transport highest, charge transfer below it with the cathodic process above the anodic, and mass transport lowest [60,61]. The transform also constrains the measurement. Because it draws on the low-frequency domain, it cannot be computed from a truncated fast-EIS sweep (Section 4.2), and a slow feature whose position follows whichever lower bound is chosen is a cut-off tail rather than a distinct relaxation.

Cyclic voltammetry (CV): CV is reported mostly as a catalyst-centric diagnostic, commonly in a three-electrode half-cell setup, rather than as a full-cell AEMEL performance benchmark. It can capture the redox-relevant potential windows during stops and holds, and the surface reconstructions triggered on restart, which are difficult to diagnose from the I–V curve alone. It is typically used to quantify the double-layer capacitance (Cdl) [47] and to track redox and oxidation-reconstruction signatures [14]. Wan et al. [14] extracted Cdl and ECSA from CV at 10 to 50 mV s^{-1} in a narrow non-faradaic window, and recorded a wider CV in which the Ni^{2+}/Ni^{3+} peaks between 1.2 and 1.6 V diminished, together with the capacitive current, after 80 groups of wind-profile cycling of a NiFe-based anode. Nam et al. [11] tested Pt-alloy HER catalysts under fluctuating start–stop protocols and quantified their dissolution after a forced reverse-current step. The authors employed RDE-style CV over a voltage window of 0.05 to 1.6 V at 50 mV s^{-1}, preceded by a preconditioning step of 50 CV scans at a fast scan rate (200 mV s^{-1}) within a narrow window of 0.005 to 0.7 V, before recording in the oxidative window. Jeon et al. [9] used CV (glassy carbon RDE, 1600 rpm, 0 to 1.55 V vs. RHE) to explain the activity losses in Ni-Mo driven by deliberate open-circuit exposure, attributing them to a surface phase transition from the metal to hydroxide and oxyhydroxide.

5. Degradation Under Intermittent Test Protocols

Each shutdown and restart forces the electrolyzer through a transient relaxation, so intermittent and start–stop operation generates degradation modes that are absent under

steady-state durability tests. The severity of that relaxation is set by three things: the charge stored in the electrodes when load is removed, the path through which that charge discharges, and the time the electrodes then remain in the discharged state. Table 4 groups the reported parameters accordingly and gives the system in which each effect was measured, so that results from liquid alkaline systems can be read against the transfer criteria of Section 3.3; these parameters are also the components of the preliminary severity vector introduced in Section 1. Figure 5 maps these severity factors onto the physical AEMEL cell architecture, identifying which component—anode catalyst layer, AEM or cathode catalyst layer—has been reported as the degradation hotspot under each stressor class discussed in Sections 5.2 and 6.

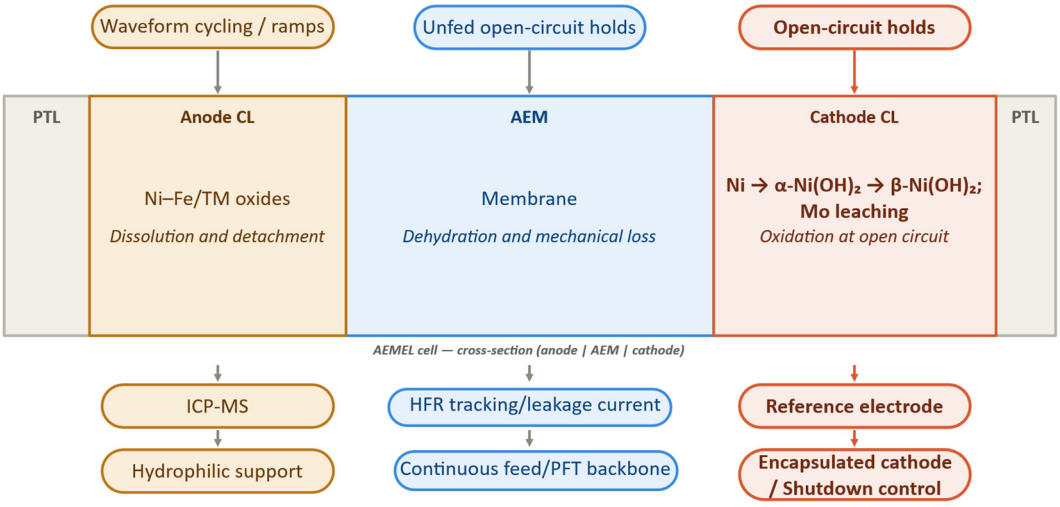


Figure 5. AEMEL cell cross-section (anode catalyst layer | AEM | cathode catalyst layer, with PTLs) mapping each stressor class to the component where degradation has been reported, with the corresponding diagnostic and mitigation. Anode: waveform cycling [14] and cold-start ramps [7]; membrane: unfed open-circuit holds [26,27] and voltage cycling [28]; cathode: open-circuit holds and forced reverse current, resolved with reference electrodes in single cells with NiFe-LDH anodes [9,11,13]. Mitigations (Section 6): hydrophilic anode support [47], continuous feed [50] and PFT membranes [28], shutdown control [8] and carbon-encapsulated cathodes [9].

Table 4. Parameters reported to change the reverse-current (discharge) event after load removal and the charge-back event on restart, grouped by what they act on: the charge stored in the electrodes, the path that carries the reverse current, and the time the electrodes remain discharged. ↑ denotes a larger reverse current or a faster or deeper discharge, and ↓ the opposite. Effects on degradation are treated in Section 5.2 and Table 5.

Parameter	Effect on Reverse Current or Discharge	System
	Charge stored (driving force)	
Prior current density	↑ Half-cell: faster self-discharge from 5 to 100 mA cm^{-2}. AEL stack: no effect over 0.4–1.0 A cm^{-2}	$Ni(OH)_2$ half-cell, 0.1 M KOH [6,55]
Electrode redox capacity and surface area	↑ Main RC source ($NiOOH \rightarrow Ni(OH)_2$); higher with Fe or Co and larger surface area. A high-capacity anode stresses the paired cathode	Half-cell; AEL stack [6,55,63]
Reactive gas inventory	AEMEL stack: ↑ Held H_2 pressure prolongs discharge. AEL stack: Dissolved gas is minor: N_2 purge had no effect; gas-free electrolyte cut reverse charge by 10–20%	AEMEL stack [8] Half-cell; AEL stack; AEL bipolar cell [6,55,63]
	Path that carries the reverse current	

Discharge route	↑ External sink: ~1.8 mA cm^{-2}, collapse in ~15 min. Internal stray current through the shared anode loop: ~0.07 mA cm^{-2}, ~6 h	AEMEL stack [8]
Position in a bipolar stack	↑ Middle cells carry the highest RC and change potential fastest	AEL stack [55]
Temperature during hold	↑ Faster redox self-discharge from 20 to 50 °C; plateau collapse after 58 min heated vs. 92 min cooled; larger RC at 80 °C than at 30 °C	Half-cell [6]; AEMEL stack [8]; AEL stack [55]
Electrolyte circulation during hold	↑ ON: collapse 49 vs. 378 min; much larger RC. OFF: gas-filled outlets raise ionic resistance ~130 → 400 Ω	AEMEL stack [8]; AEL stack [55]
Electrolyte concentration	Half-cell (reaction-limited): ↓ 0.1 → 7 M KOH slows redox self-discharge. AEMEL stack (path-limited): discharge slowest near 1 wt % KOH, faster above it (more conductive stray path) and below it (reduced usable capacity)	Half-cell [6]; AEMEL stack [8]
Exposure (time the electrodes stay discharged)		
Hold duration relative to discharge time	↑ Holds beyond plateau collapse give full discharge; restart at 1.2 V avoids it	AEMEL stack [8]
Restart after discharge (charge-back)	Re-oxidation at M^{2+}/M^{3+} releases dissolution bursts (Co spikes)	Half-cell, flow cell [6]

Table 5. Reported AEMEL degradation under intermittent protocols, normalized to a common per-cycle basis. Per-cycle rates are not comparable without the cycle period and the current density at which the loss was measured, both of which are given. Evidence type distinguishes electrode-resolved measurement from full-cell inference.

Study (Scale)	Stop Regime; Cycle Period	Normalized Rate	Measured at	Evidence
Galkina et al. [10], (single cell, 60 °C)	Continuous operation, no stop; 1000 h	84 μV h^{-1} from the 200 h minimum; 45 μV h^{-1} overall BOT to EOT	1 A cm^{-2}	Full-cell
Jeon et al. [9], Ni_3Mo (single cell, 60 μm AEM, 50 °C)	Passive true-OCV, 30 min; 1 h cycle	6.7 mV $cycle^{-1}$ (48 cycles); same cell under continuous load 1.25 mV h^{-1} (24 h)	1 A cm^{-2}	Electrode-resolved
Jeon et al. [9], $Ni_3Mo@C_{60}$ (as above)	Passive true-OCV, 30 min; 1 h cycle	0.73 mV $cycle^{-1}$ (192 cycles)	1 A cm^{-2}	Electrode-resolved
Nam et al. [11], Pt alloys (single cell, 50 °C)	Passive true-OCV, 1 h; 2 h cycle, 50 h	No significant rise for PtNi/C, PtCo/C, PtRu/C or Pt/C	1 A cm^{-2}	Full-cell
Guruprasad et al. [13], (single cell, 5 cm^2, 60 °C)	Forced polarity inversion, 0.03 A cm^{-2}, 30 min; single event	+1.7 V NiMo/C; +0.20 V PtRu/C; +0.05 V Pt/C	1.5 A cm^{-2}; electrode-resolved only ≤0.2 A cm^{-2}	Electrode-resolved and full-cell
Gladik et al. [8], (stack, 22 × 60 cm^2, 50 °C)	External discharge to 0 V, 40 min; ~1 h cycle	0.337 mV $cycle^{-1}$ heated; 0.026 mV $cycle^{-1}$ cooled; −0.043 mV $cycle^{-1}$ at 20 min cooled (60 cycles each)	0.85 A cm^{-2}	Full-cell
Niaz et al. [26], (single cell, 6.25 cm^2, 50 °C)	Passive true-OCV, 12 h, unfed; ~100 h between rests	HFR 0.101 to 0.227 Ω cm^2 over 1000 h; fed control stable over 800 h [50].	1.95 V (cycle peak)	Full-cell with ex situ membrane conductivity
Wan et al. [14], (single cell, 80 °C)	Waveform cycling 1.50 to 1.70 V, never reaches open circuit; 1000 s cycle	0.17 mV $cycle^{-1}$ (30 mV over 180 cycles, 50 h)	0.5 A cm^{-2}	Full-cell
Motealleh et al. [12], (single cell, 5 cm^2, 60 °C)	Low-bias hold at 0.02 A cm^{-2}, never reaches open circuit; 4 s cycle	0.00015 mV $cycle^{-1}$ virgin; 0.00165 mV $cycle^{-1}$ with 2 wt % ZrO_2 (11,000 cycles)	2.4 A cm^{-2} (cycle peak)	Full-cell

5.1. Shutdown Transient: Reverse Current and Voltage Collapse

When the load is removed, the cell voltage falls first through the instantaneous ohmic (iR) drop and then decays as the electrode potentials equalize. The driving force is the charge stored in the double layers and in surface redox states, supplemented by H_2 and O_2 retained in the porous catalyst layers, electrodes and manifolds. While an ionic path still connects the electrodes, this charge sustains a self-discharge, or internal reverse

current (RC), that drives the cell voltage down [13,49]. The parameters reported to change this event are grouped in Table 4. The mechanism is established in liquid alkaline systems and is transferred here on the surface-chemistry grounds of Section 3.3, without its magnitudes. In an alkaline half-cell, a capacitive discharge on the millisecond scale was followed by the slower redox self-discharge of NiOOH to $Ni(OH)_2$, a feature between ~1.4 and 0.9 V vs. RHE that persisted for ~13 s before the potential decayed further [6]. In bipolar alkaline cells, the reverse current was dominated by Ni-surface redox rather than by dissolved gas [63]. These AEL findings are relevant to AEMEL because electrolyte-fed AEMEL stacks also share a conductive KOH feed through joined manifolds; the 1 M KOH used is less conductive than the 6–7 M of AEL, but AEMEL stacks do not yet use the inlet designs with which AEL stacks minimize shunt currents [13].

Shutdown proceeds either by internal discharge, through the ionic path that remains in the cell or stack, or by external discharge, through the external electrical circuit, in which a power supply left connected to the stack acts as a current sink [8]. The route sets the magnitude of the reverse current and how quickly the voltage plateau collapses (Table 4), and therefore how long the cells spend at low voltage. Whether that time causes damage depends on the temperature and duration of the dwell at 0 V that follows (Figure 6; Section 5.2.3).

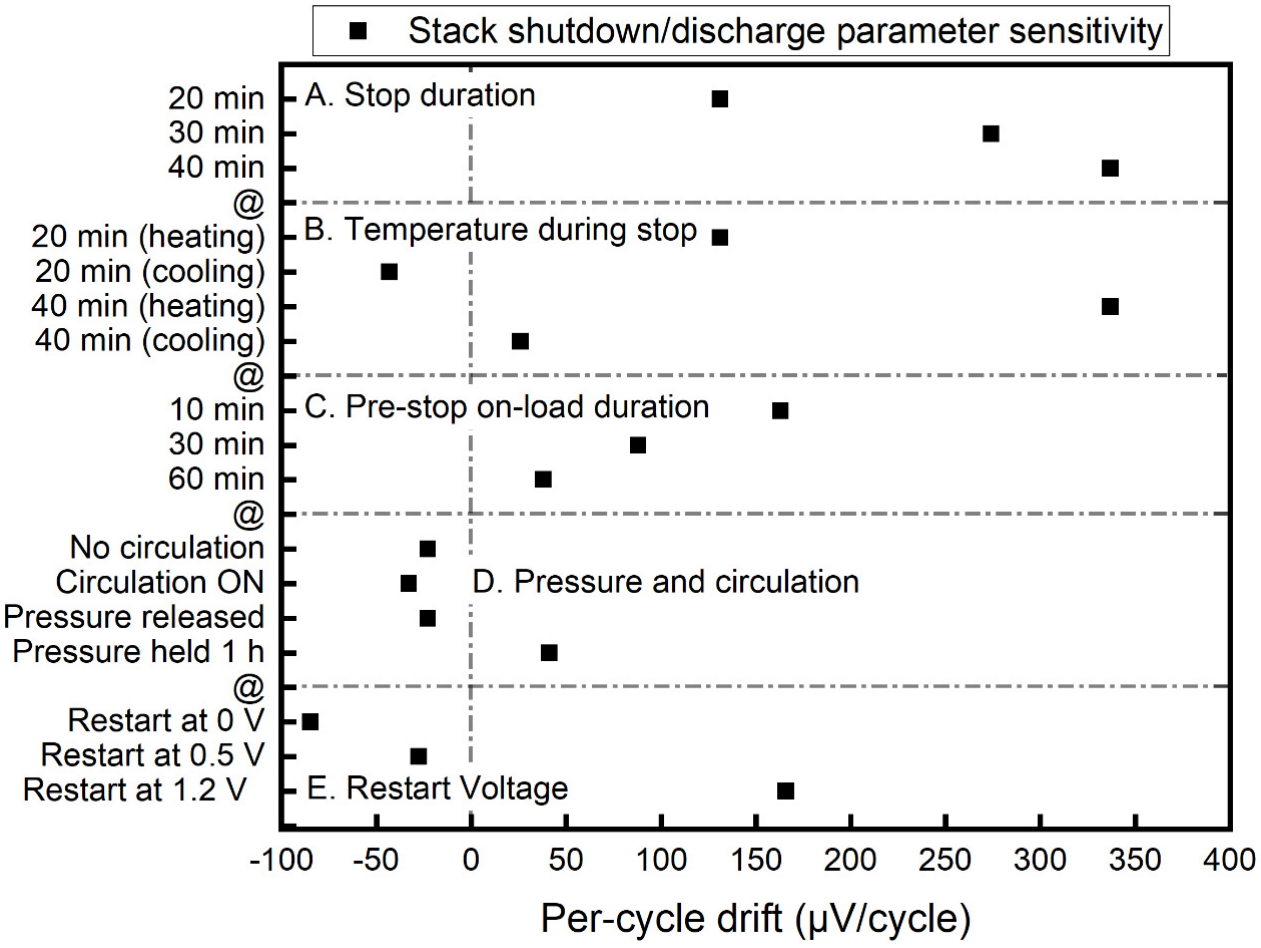


Figure 6. Per-cycle voltage drift of a 22-cell, 60 cm^2 AEMEL stack under systematic variation of the shutdown conditions, each from 60 shutdown cycles after 30 min at 0.85 A cm^{-2}: (A) external discharge duration at 50 °C; (B) stack temperature during the stop, heated to 50 °C or cooled; (C) operating time before the stop; (D) hydrogen pressure and electrolyte circulation during the stop; (E) lower voltage limit at which the stack is restarted. Positive values denote an increase in cell

voltage per cycle (degradation), negative values a decrease (regeneration). Replotted by the authors from digitized values in [8].

AEL and AEMEL differ primarily in ionic path length and in the available shunt pathways. Conductivity is much lower in an AEMEL system because of the lower-concentration electrolyte, <1 M (AEMEL) against 6–7 M (AEL) [63,68]. AEMEL stack designs, however, may not yet implement the mature shunt-current mitigation strategies practiced in AEL.

Loss of cathodic protection explains why open-circuit holds load the cathode in the cells resolved so far. Hydrogen evolution keeps the cathode near the reversible hydrogen potential while current flows, and residual hydrogen in the catalyst layer keeps it pinned there for a time after the bias is removed, but that inventory is finite. As it is consumed, and with oxygen crossing the membrane, the electrode comes to rest at a mixed potential set by hydrogen oxidation competing against oxygen reduction. Where that potential settles depends on the catalyst: a non-precious HER surface has a far lower hydrogen oxidation exchange current density than Pt, so the pinning is weak, the potential shifts anodically once residual hydrogen runs out, and the Ni surface leaves its immunity region for the hydroxide and oxyhydroxide window. A fast hydrogen oxidation reaction instead holds a Pt/C cathode near 0 V vs. RHE while hydrogen remains, and Pt is stable over a wider potential window than Ni or Ni-Mo, consistent with the catalyst ordering under forced reversal (Section 6.3). Each open-circuit hold is therefore a repeated anodic excursion of the cathode, the drift resolved on a Ni_3Mo cathode in Figure 7a. Metallic Ni can convert spontaneously to α-$Ni(OH)_2$ at open circuit and age irreversibly to HER-inactive β-$Ni(OH)_2$ [9]. For Ni-Mo the window adds Mo instability: Pourbaix analysis places the decomposition of Ni_3Mo to MoO_2 around OCP, and to molybdate and $Ni(OH)_2$ above 0 V vs. RHE, and identifies the thermodynamic driving force at OCP as the origin of the dissolution of non-precious HER catalysts, confirmed by ICP-MS for catalysts in acid [13,69]. In AEL, a Raney Ni cathode rose to about +0.2 V vs. RHE after shutdown, and cathode loss has been attributed to poorly conducting oxygen-containing products and, in Ni alloys, to dissolution of the alloying element, with repeated redox cycling preventing a passivating (oxy)hydroxide from persisting [70]. At stack level, Gladik et al. [8] proposed a similar sequence at the Pt-containing electrode: once hydrogen is depleted at 0 V, contaminants or electrode components are oxidized instead, a temperature-activated reaction that the authors regarded as not yet identified.

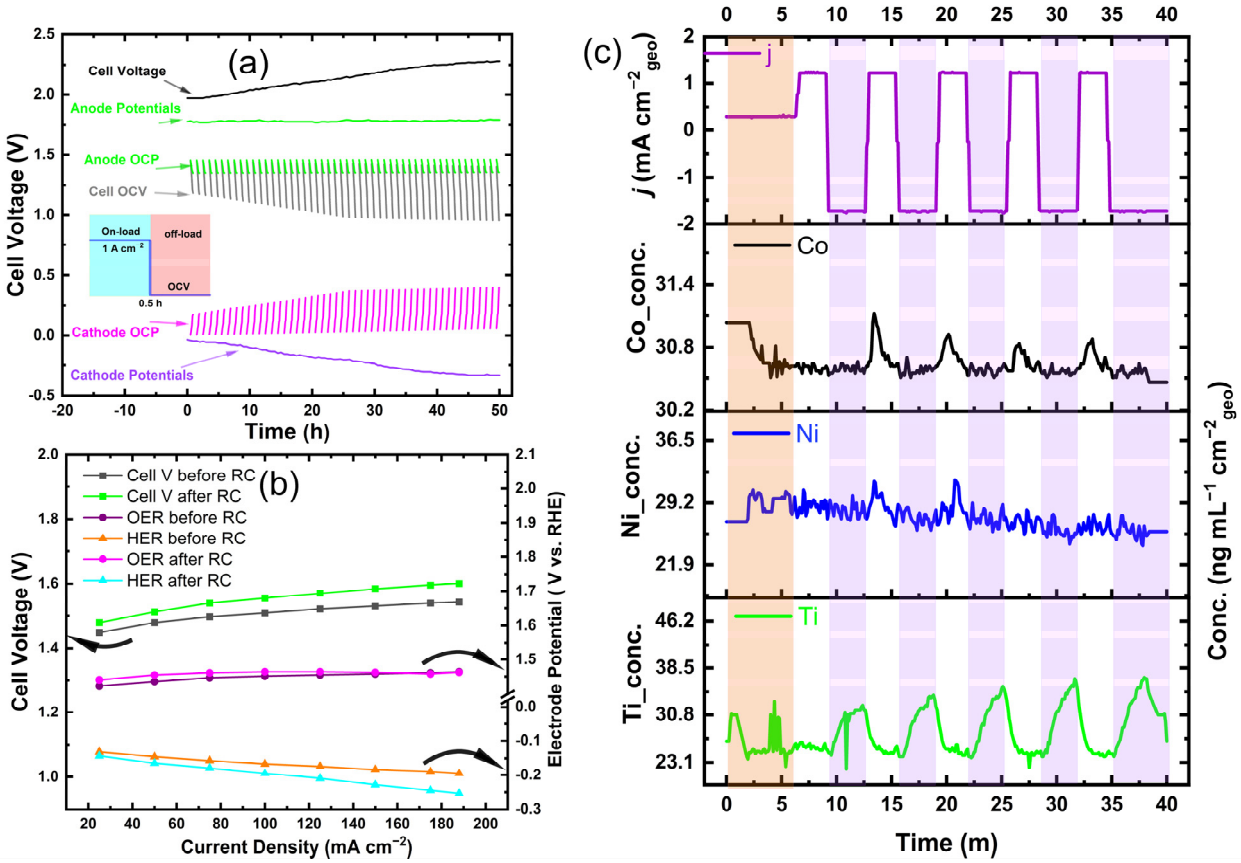


Figure 7. Electrode-resolved degradation under intermittent operation. (**a**) Cell voltage and electrode potentials under start–stop cycling (1 to 0 A cm^{-2}, 30 min steps) over 48 h [9]. (**b**) Cell, anode and cathode polarization before and after 30 min of reverse polarization, measured against a cathode-side reference electrode [13]. (**c**) Current-density steps (±1.35 mA cm^{-2}) applied to a Ti-foil-supported $NiCo(OH)_2$ electrode in 0.1 M KOH, with dissolved Co, Ni and Ti tracked by online ICP-MS; orange: preconditioning step; purple: reverse-current steps [6]. All panels replotted by the authors from digitized values in the cited works.

5.2. Protocol-Specific Degradation Signatures

Intermittent test protocols can be grouped by protocol class, and each class produces a distinct degradation signature. Table 5 collects the reported rates across these classes on a common basis, and Section 5.3 reads them together.

5.2.1. Waveform Cycling

This potential-driven waveform intermittency is commonly adopted in laboratory-scale tests across electrolysis technologies. Narayanaru et al. [28] applied 2.0 to 0.1 V cycling (1000 cycles, 2 min cycle time) and showed a strong dependence on AEM and ionomer chemistry: PFT-based membranes and ionomers retained performance, whereas Sustainion exhibited pronounced chemical and mechanical loss, indicating that the AEM and the catalyst layer are vulnerable to repetitive high-frequency voltage waveform cycling. Ul Hassan et al. [46] further showed that square and triangular waveform cycling between 1.45 and 2 V redistributes stress between catalyst-layer-dominated degradation (ionomer oxidation, catalyst detachment) and changes in ohmic pathways (HFR improved by membrane thinning). Waveform-induced degradation was reported to be more severe in DI water, which the authors attributed to its lower ionic conductivity, and at the harsher 1.80 V upper voltage [47]. Recent waveform data support a more general trend. Wan et al. [14] found that, at equal 50 h ADT duration between 1.5 and 1.7 V on $Ni_xFe_{1-x}S$, shorter

step intervals produced systematically larger losses: catalyst-layer thinning of 22.95% at 200 s, 11.24% at 500 s and 8.19% at 1500 s, and Ni dissolution of 6.561 versus 0.148 mg L^{-1} between 200 s and 1500 s, more than a 40-fold difference at identical accumulated test time. The authors attributed the irreversible loss to collapse, dissolution and agglomeration of catalyst particles, and the reversible loss to gas retained in the porous catalyst layer, which a rest period partly recovered.

5.2.2. Start–Stop Cycling: Polarity-Inversion Discharge and Open-Circuit Holds

Start–stop operation opens a stability window that steady galvanostatic operation rarely reaches. This window can drive the electrodes into potential regimes that are chemically aggressive for the catalysts, the supports and the interfaces, promoting oxidation, phase transformation and dissolution pathways that are not sampled under steady-state load. At the Ni-based oxygen electrode, a key pathway is the reduction of oxidized NiOOH states back towards $Ni(OH)_2$ states during discharge, while the catalyst at the hydrogen electrode is instead oxidized. Marquez et al. [6], in a LAEL (liquid alkaline electrolyzer) half-cell study, connected deep discharge (an imposed reverse current density) to the formation of a mixed hydroxide and metallic phase. Imposing a reverse-current discharge (−0.25 mA cm^{-2}) on a $Ni(OH)_2$-deposited electrode produced distinct stages. The stages identified and subsequently confirmed by in situ SERS (Raman) were (i) at ~0.8 V vs. RHE (Ni^{2+}/Ni^{3+}), Raman spectra (~476/558 cm^{-1}) retained a strong oxyhydroxide (NiOOH) signature in this early window; (ii) between 0.6 and 0.2 V vs. RHE, hydroxide bands emerged (~463/477 and 694 cm^{-1}), indicating NiOOH to $Ni(OH)_2$ conversion during progressive reduction; and (iii) a sharp potential drop to −0.2 V vs. RHE followed by stabilization, which the authors interpreted as further reduction to a more metallic state at deep discharge [6]. The same approach applied to $NiCo(OH)_2$ and $NiFe(OH)_2$ films showed the oxyhydroxide phase reappearing under OER potential and producing repetitive hydroxide bands at the OCP reverse step. Critically, deep discharge of the electrode in this sequence introduces a metallic-phase signature and leaves the oxyhydroxide only partially recovered in the OER steps that follow. Online ICP-MS coupled to an electrochemical flow cell resolves elemental loss in real time (Figure 7c). Dissolved Co spikes reproducibly during film reoxidation, at the M^{2+} to M^{3+} transition, whereas Ni declines gradually along a baseline with weaker reoxidation-linked features—a signature of corrosion bursts driven by redox cycling and phase transitions, rather than of dissolution dominated by the steady OER segments. Ti-support dissolution behaves differently, rising during the discharge portions of the cycle, which points to reduction of the Ti-oxide passivation layer under reverse current and partial re-passivation once oxidizing conditions return.

AEMEL systems reach the same chemistry through shutdown at true open circuit rather than through explicit polarity inversion. Three AEMEL single-cell studies have resolved the electrode potentials under such stressors. Under passive open-circuit hold, Jeon et al. [9] cycled a cell between 30 min at 1 A cm^{-2} and 30 min at open circuit with a cathode-side reference electrode; the cathode potential drifted anodically during each hold as metallic Ni-Mo converted to less active hydroxide phases, while the anode OCP remained stable (Figure 7a). Under forced inversion at 0.03 A cm^{-2} for 30 min, Guruprasad et al. [13] assigned ~50 mV of the ~55 mV cell-voltage loss at 0.2 A cm^{-2} on PtRu/C to the cathode (Figure 7b), and Mo dissolution from NiMo/C rose from ~37% after steady operation to ~88%. Nam et al. [11] applied the same inversion to four Pt-based cathodes and found the anode potential nearly unchanged while the cathode potential shifted, most for PtRu/C and least for PtNi/C. Under passive open-circuit holds, the same Pt-alloy cathodes showed no significant loss, so for PGM cathodes the localization has been shown only under forced inversion.

These results establish a cathode-dominated loss under open-circuit and reverse-current stressors for the electrode pairs tested, not for AEMEL in general. All three studies compared cathode catalysts against a fixed NiFe-LDH anode, so anode stability is established for that chemistry only, and studies designed the other way locate the loss elsewhere. Wan et al. [14] varied NiFe-based anodes against a Pt/C cathode under waveform cycling that never reached open circuit and attributed the loss to anode thinning and dissolution, inferred from full-cell and post mortem data. In AEL half-cells, Ni- and Co-based anode films tolerated open-circuit rests but degraded by several hundred mV h^{-1} under a deliberately exaggerated reverse current [6], so anode stability depends on the stressor as well as the material. At stack level, impedance fitting shows no cathode preference: the arc assigned to the OER grew almost twice as much as the HER arc over 925 cold starts [7], and over ~1300 shutdowns to 0 V the two arcs grew comparably while the ohmic resistance rose most [8]. These assignments are preliminary, but the cathode-dominated picture rests on single cells and has not been shown in a stack.

Niaz et al. [26,27] reported that frequent short dry open-circuit holds can cause an irreversible increase in high-frequency resistance (HFR) in AEMEL, whereas longer, less frequent holds produce much smaller ohmic drift. Section 6.1 notes that this irreversibility may reflect cation loss at low hydration rather than dehydration alone. In contrast, the same authors in a later study [50] reported that open-circuit holds under electrolyte feeding preserved the ohmic resistance over ~800 h but introduced a transient, fully reversible polarization increase after each hold. The authors attributed this to "excess feed solution" and did not consider reverse current. The signature is fully reversible and appears only when a continuous ionic pathway is maintained across the cell. An alternative interpretation the study did not test is a reverse-current contribution during shutdown and restart; distinguishing the two would require the cathode potential to be tracked through the idle interval. Motealleh et al. [12] reported very low per-cycle drift under 11,000 pulse cycles, but at a 0.02 A cm^{-2} lower bound that never reaches open circuit, as did a cell cycled to a 0.005 A cm^{-2} bound [51].

5.2.3. Stack-Level Shutdown

Systematic stack-level evidence on how the stop is executed comes almost entirely from one AEMEL system, a 22-cell stack tested by Gladik et al. [8]. Their per-cycle drift varied by more than an order of magnitude with how the stop was executed, and Figure 6 compiles it across the five parameter groups tested [8]. The decisive variable was not how deeply the stack was discharged but how long it then stayed at low voltage. Restarting at 1.2 V, before the voltage plateau collapsed, left the reversible loss accumulated during operation in place, whereas restarting at 0.5 V or immediately on reaching 0 V regenerated it, which the authors linked to hydrogen depletion at the Pt-containing electrode (group E). Remaining at 0 V at 50 °C had the opposite effect: longer external discharge raised the drift to 337 μV $cycle^{-1}$ at 40 min, with a rise that flattened between 30 and 40 min (group A). The authors attributed this damage to a thermally activated process at low cell voltage, and cooling during the stop cut the 40 min rate to 26 μV $cycle^{-1}$ (group B). Longer operation between stops also lowered the drift (group C), and maintained hydrogen pressure was the only balance-of-plant parameter that raised it (group D). Electrolyte circulation and discharge route changed how fast the stack discharged (Table 3) but not the degradation, so they set the duration of the low-voltage window rather than the damage within it. This stack result appears to contradict the irreversible ohmic loss reported for an unfed single-cell hold [26,27]; Section 5.3 reconciles the two.

These rates carry a direct penalty in output. At one deep stop per day, the 337 μV $cycle^{-1}$ of a heated 40 min hold at 0 V [8] averages 14 μV h^{-1} over the day, which alone

consumes almost the whole 2030 target of below 15 μV h^{-1} set for AEMEL stacks [71], a target specified for degradation during operation rather than for stops [7]. The cooled hold, at 26 μV $cycle^{-1}$, uses about 7% of the same budget. Expressed as output, a year of daily deep stops adds 123 mV to the cell voltage, some 3.3 kWh per kilogram of hydrogen against a specific energy consumption near 50 kWh kg^{-1}. The comparison assumes one stop per day, and the most severe condition tested, but it shows that the shutdown protocol alone can decide whether a stack meets its degradation target.

5.2.4. PV- and Wind-like Profiles and Irregular Fluctuations

Beyond binary on–off switching, renewable-derived profiles introduce fluctuations under which part of the performance change is reversible, arising from transport limitation and gas holdup, and part is irreversible, arising from catalyst and structural evolution. Wan et al. [14] modulated 24 h wind-power fluctuations by scaling down the output of an actual 10 kW wind turbine. The protocol comprised a periodic waveform between 1.2 and 1.8 V for 80 groups, with a 100 h rest period after 40 groups. The major irreversible loss occurred in the first 10 groups and was attributed to lower ECSA and higher charge-transfer resistance arising from dissolution, detachment and agglomeration. After the 100 h rest, part of the performance loss proved reversible, amounting to about 6% of the current, indicating that gas stagnation in the porous catalyst layer temporarily blocked electrolyte access to the active sites and led to higher polarization.

5.3. Synthesis: Normalized Rates and Reconciled Evidence

Normalization exposes a spread of more than four orders of magnitude, most of which is attributable to protocol rather than to material. Cycle period accounts for part of the range, since a 4 s pulse and a 1 h start–stop differ by three orders of magnitude in cycle count over the same elapsed time, so per-cycle rates cannot be compared without it. The depth of the stop accounts for more: protocols that never reach open circuit sit at the bottom of the range [51], and those holding at 0 V at operating temperature sit at the top. Two comparisons isolate the effect. On one cell, a Ni_3Mo cathode drifted at 1.25 mV h^{-1} under continuous load but lost 6.7 mV per cycle under hourly open-circuit holds [9], so the stop rather than the operation accounts for the loss. Under a comparable open-circuit protocol at the same temperature, Pt-alloy cathodes showed no significant rise, so the magnitude of that loss is set by the stability of the cathode metal rather than by the stressor alone. Forced polarity inversion is reported separately as an upper bound, because it is an imposed stress rather than an operating state.

One apparent conflict in the reviewed evidence is worth resolving. At stack level, electrolyte circulation during the hold made no measurable difference to per-cycle drift [8], whereas in single cells an unfed hold drove an irreversible ohmic rise [27]. The two findings are not in conflict, because the same word covers different variables. A stack retains a liquid inventory in its manifolds and cells, so the membrane stays hydrated whether the pump runs or not, and circulation governs only the ionic path available to the reverse current. In a single cell with the feed stopped, the membrane electrode assembly dries. Neither result therefore transfers to the other scale: the stack finding does not license an unfed hold in a single cell, and the single-cell finding does not predict stack behavior.

6. Mitigation Strategies

6.1. Operational Strategies

An operational measure changes no materials and no BoP hardware. It changes the protocol: how the cell is taken down to standby, what state it occupies while idle, and how it is brought back to load. Four such levers have been demonstrated, either in AEMEL

itself or in AEL and PEMEL work whose transfer is licensed by the criteria in Section 3.3, on hardware ranging from single cells to multi-cell stacks.

Standby state: A small protective current (pseudo-OCV, or low-bias standby) holds the electrode potentials inside a safer polarization window than a pure open-circuit hold allows, suppressing the mixed-potential and reverse-redox processes behind cathode dissolution and membrane stress [72]. PV-mimic accelerated testing bears this out: a protective current of 0.3 A cm^{-2} during low-power windows brought the degradation rate from ~11 mV h^{-1} at OCV down to ~3 mV h^{-1}, roughly a fourfold improvement [72]. The evidence is strongest in PEMEL [72], is accumulating in AEMEL, and sits well with the Pourbaix-stability argument for non-precious HER catalysts at OCP [69]. The costs are parasitic power and a more complex BoP control scheme. How small that current can be and still protect an AEMEL cathode has not been mapped across catalyst chemistries.

Electrolyte management during standby: The lever here is continuous feed at an intermediate concentration. Dry open-circuit holds have emerged as a key stressor in long-running AEMEL durability tests, producing an ohmic rise that does not recover on resumption of feed. Niaz et al. quantified it with a paired design—same MEA, same cell hardware, differing only in electrolyte feeding. Dry open-circuit holds every ~100 h drove ohmic HFR from 0.101 → 0.227 Ω cm^2 over ~1000 h [26]; continuous KOH feed under identical 12 h open-circuit holds held it essentially constant over ~800 h [50]. Dehydration alone cannot account for this, since it reverses on rehydration; an irreversible residue implies lost fixed-charge sites. At low water content the hydroxide ion is poorly solvated and more nucleophilic, accelerating attack on the quaternary ammonium cation by nucleophilic substitution and Hofmann elimination [22,73], and separating the two mechanisms would require ion-exchange capacity measured after full rehydration. Concentration is the second axis of this lever. Dynamic square-wave tests gave systematically larger per-cycle penalties in 0.1 M KOH and in pure water than in 1 M KOH [47], and ~2000 h of AEMEL operation with recirculated electrolyte put the optimum at 0.5–1 M KOH, balancing ionic conductivity, mass transport and crossover [53]. None of this is free. Continuous KOH feed during standby forfeits the pure-water or ultra-dilute operation that distinguishes AEMEL (Section 2.2), consumes pump energy, opens shunt-current pathways at stack level, and lets carbonate form if air enters the BoP during a stop. The Niaz studies also used single 6.25 cm^2 MEAs and have not been confirmed in multi-cell stacks. Whether minimum-flow standby, reduced but non-zero, captures most of the benefit at lower parasitic cost is open.

Shutdown transient control: The variables are ramp slope, hold duration and cooling, and of the operational levers shutdown management has the strongest stack-level evidence behind it. On a 19-cell, 60 cm^2 stack, Gladik et al. [7] shortened the cold-start ramp from 120 s to 12 s, raising per-start degradation from 10–11 to 15–26 μV $start^{-1}$ in their 150-cycle confirmation series. Damage followed the current slope (dI/dt), not the peak voltage. In a companion stack study, shutdown temperature and 0 V hold duration proved more consequential still: cooling the stack through a 40 min hold cut per-cycle drift by over 92%, and a shorter cooled hold produced net regeneration rather than damage (Section 5.2.3) [8]. In an AEL stack, circulation narrowed the "safe shutdown window" from ~50 to ~12 min by lowering the ionic resistance [55]; in the AEMEL stack it changed the discharge rate but not the per-cycle drift [8]. Both measures carry costs. Moderate ramping costs availability for fast renewable following, and cooling demands thermal infrastructure while working against the warm state an efficient restart wants [44]. Studies so far have varied each lever on its own, so the joint optimum between ramp time, hold time and cooling depth under a realistic intermittent profile is still unknown.

Waveform engineering: Where the load profile is itself a design variable, through storage buffering or controller logic, its shape becomes a protection lever. Ul Hassan et al.

[46] showed that square waveforms stress the catalyst-layer ionomer preferentially and promote catalyst detachment, while triangular waveforms shift the burden toward membrane thinning. Smoothing the transitions therefore moves stress away from the catalyst-layer interfaces that abrupt square-wave steps load. The lever needs a controllable BoP, which a raw directly coupled renewable source does not provide. Intermediate shapes, trapezoidal and ramped-pulse profiles among them, have not been tested systematically in AEMEL.

Of these four levers, shutdown control carries the strongest quantitative evidence, at stack level [7,8] followed by electrolyte feeding at single-cell level [26,50]. Protective-current standby and waveform shaping are sound in principle and still await confirmation at stack scale in AEMEL [74].

6.2. System-Level Strategies

System-level measures act at the BoP and control layers, not at the cell. They become essential once AEMEL is integrated into a stack and a renewable-coupled power system. Four recur in the literature, each trading added complexity against durability gain.

Minimum-load and minimum-run-time policies: Every avoided stop eliminates a degradation cycle outright, which makes these the cheapest mitigations available. Ursúa et al. [15] noted that commercial alkaline stacks already ship with a manufacturer-imposed lifetime cap of ~5000 start–stop cycles and known performance liabilities below 25% of rated load. Control logic that enforces a minimum load and a minimum run-time before any shutdown reduces the stop count in PV and wind simulations by an order of magnitude [15]. The cost is energy curtailed during low-power windows; the gain depends on the lifetime cost of the avoided cycles. For PEMEL, including use-dependent degradation raised the levelized cost of hydrogen from \$4.56 to \$6.60 kg^{-1} [75], but no equivalent estimate exists for AEMEL.

Energy storage buffering: The same problem can be addressed with hardware rather than policy. A battery or supercapacitor bank between the renewable source and the AEMEL absorbs short transients, smoothing the load profile and avoiding both deep ramps and unwanted stops. Sun et al. [76] demonstrated a proof-of-concept PV–Li-ion–AWE integrated system in which the battery provided a stable ~0.45 A output to an alkaline electrolyzer for >12 h despite intermittent solar input; the study was motivated primarily by gas-crossover concerns at partial loading. The trade-off between durability gain and storage cost remains among the least quantified BoP levers in the AEMEL literature.

Stack-scale shunt-current management: This lever becomes critical once continuous electrolyte feeding (Section 6.1) is implemented in a multi-cell stack, because the same electrolyte path that protects the membrane also carries reverse and shunt currents through the manifold. Guruprasad et al. [13] weighed polarization rectifiers in the BoP, which add capital cost and can compromise gas purity, noted that AEMEL stacks do not yet use the shunt-minimizing inlet designs of alkaline stacks, and called for modelling and stack-level validation of reverse-current magnitudes. Protection can also be applied at the electrode. Kim et al. [49] coupled sacrificial metals (Pb, Zn, Sn, Al) galvanically to the Ni cathode and raised the reverse-current stability factor from ~73% to 97–100%, removing the ~75 mV overpotential rise that an unprotected RC event leaves behind. The demonstration is in AEL, but Ni-based HER catalysts in a zero-gap AEMEL are vulnerable to the same oxidation pathway at open circuit, so the principle may carry across.

Integrated diagnostics for adaptive control: Ranz et al. [59,77] distinguished catalyst-layer from membrane failure modes using time-resolved EIS alongside leakage-current tests at 1.3 V, and online ICP-MS at the outlet of a flow cell [6] tracks dissolution online as a complement. Once an early failure signature is detected, the shutdown procedure, the

protective-current setpoint and the minimum-load threshold can all be tightened in response. Integration is what is missing: no published AEMEL study has yet demonstrated closed-loop control that adjusts protocol parameters from live diagnostic signals.

Gas purity constrains all these levers, and it does so in the same direction as durability. Hydrogen crossover is driven by partial pressure and is largely independent of load, whereas oxygen production falls with current, so the hydrogen fraction in the anode stream rises steeply as load falls and is unbounded at open circuit. A protective standby current maintains the oxygen flow that dilutes it, which sets a floor on how small that current can usefully be; minimum-load limits are imposed for this reason as much as for efficiency; and a stop held under hydrogen pressure accumulates crossover hydrogen in a static anode compartment. Gladik et al. designed their stack shutdown accordingly, releasing hydrogen pressure before the current ramp specifically to avoid an explosive mixture at the oxygen outlet, and the same release moved per-cycle drift from +41 to −23 μV cycle^{-1} [8]. Safety and durability therefore recommend the same stop procedure.

6.3. Materials Strategies

Materials measures act on the cell components themselves—membrane, catalyst, support, interfaces—rather than on the protocol or the system around them. Three design axes have produced durability gains in AEMEL or in AEL work of direct relevance, though not every one of them has been tested under intermittent operation specifically.

Membrane and ionomer chemistry: Narayanaru et al. [28] compared polyfluorene-based (PFT-C10-TMA) AEMs with imidazolium-based Sustainion X37-50 over 1000 cycles of 2.0 ↔ 0.1 V at 80 °C. The PFT-based MEAs retained performance; the Sustainion-based MEAs leached catalyst and lost the membrane chemically and mechanically. Mechanical reinforcement acts on a different axis. Motealleh et al. [12] cycled virgin and 2 wt % zirconia-reinforced Sustainion X37-50 between 0.02 and 2.4 A cm^{-2} for 11,000 cycles and reported 1.65 μV cycle^{-1} for the reinforced membrane against 0.15 μV cycle^{-1} for the virgin material, while reinforcement raised impact strength by 57% and lowered the hydrogen crossover current from 0.075 to 0.033 mA cm^{-2}. Both drift rates are low in absolute terms, so the trade-off is a modest efficiency penalty set against mechanical integrity and improved gas separation rather than a durability gain in itself. FAA-3-50 fails differently, and with temperature: Ranz et al. [77] watched leakage current at 1.3 V climb from ~1 mA cm^{-2} to over 100 mA cm^{-2} as the membrane broke down at 70 °C over 155 h. That sets an upper operating-temperature limit which an intermittency-tolerant design must respect.

Cathode HER catalyst selection: Cathode oxidation driven by reverse current and by open-circuit holds is the most consistently reported failure mode, which makes cathode catalyst choice the materials decision with the greatest effect on durability. Guruprasad et al. [13] tested three HER catalysts under polarity-inversion conditions (0.03 A cm^{-2} for 30 min): the cell-voltage rise measured at 1.5 A cm^{-2} was ~+0.05 V for Pt/C, ~+0.20 V for PtRu/C, and ~+1.7 V for NiMo/C. The ordering reflects intrinsic resistance to anodic excursions: Pt is thermodynamically stable across a wider potential window than the non-precious alternatives. Wang et al. [69] quantified this in acid: MoS_2, MoP and CoP dissolved about an order of magnitude faster at OCP than during hydrogen evolution, and Pourbaix analysis predicts the same for Ni_3Mo in base, which OCP places outside its stability window. Carbon encapsulation and matrix integration have both been proposed as routes to retaining non-precious catalysts. For the first, Jeon et al. [9] reported that $Ni_3Mo@C_{60}$ held the cell voltage rise to +0.14 V after 192 cycles where bare Ni_3Mo reached +0.32 V after 48, and attributed the difference to a carbon shell suppressing OH^- ingress and the volumetric lattice expansion that metal-to-hydroxide conversion requires.

Anode architecture and bubble management: Support and electrode-architecture choices can mitigate the anode dissolution reported under waveform cycling (Section 5.2). Shaik et al. [47] reported ~0.20 mV h^{-1} at 0.5 A cm^{-2} over 1500 h for super-hydrophilic TiO_2-nanotube supports carrying NiFe (NiFe/ATNT), along with a small per-cycle current loss in square-wave tests between 0.10 V and 1.60 or 1.80 V, outperforming hydrophobic Ti-felt-based electrodes. Rapid bubble release is the mechanism: residual O_2 never gets trapped in the anode catalyst at shutdown, which slows the reverse reaction. Kuang et al. [48] found the same principle at work in AEL, where tape-cast self-supported Ni/$Ni(OH)_2$ electrodes showed no appreciable additional overpotential and lower Ni^{2+} dissolution than Raney Ni after 7-min-on/7-min-off start–stop cycling, attributed to a hierarchical porous structure that improves bubble release and electrode-membrane contact. Firm anchoring is a second route: a pyrolyzed, Li-doped NiFeCo oxide bonded to Ni felt leached less Ni than its undoped counterpart and, paired with a Pt/C cathode in an AEMEL, showed negligible loss over 3000 start/stop cycles of 60 s, with the stop state unspecified [78].

Intermittency-specific evidence is strongest for PFT-based AEMs, zirconia-reinforced membranes, Pt/C cathodes under RC stress, super-hydrophilic anode supports under waveform cycling, and Cr-promoted NiFe oxyhydroxide anodes under fluctuating load at stack scale [52]. $Ni_3Mo@C_{60}$ is promising on a shorter record: hundreds of cycles, where thousands are the relevant number. High-current-validated architectures (Int-Ni/MoO_2; CAPist-L1) and a head-to-head intermittent-protocol comparison across materials axes remain absent from the AEMEL literature [79].

6.4. Comparison and Trade-Offs

The mitigations discussed across Sections 6.1–6.3 differ widely in evidence quality, scale of demonstration, and target failure mode. Table 6 summarizes the best-evidenced lever in each category, the headline durability result, and the principal remaining gap.

Table 6. Strongest-evidenced AEMEL mitigation strategies under intermittent operation, by category. Headline result cites the original study; evidence scale (single cell, stack, AEL precedent) is indicated where relevant.

Category	Strongest-Evidenced Lever	Headline Result	Principal Remaining Gap
Operational	Shutdown cooling + short 0 V hold	337 → 26 μV $cycle^{-1}$ at 40 min hold; −43 μV $cycle^{-1}$ at 20 min cooled; stack, [8]	Combined optimum of ramp + hold + cooling under realistic profiles not yet mapped
Operational	Continuous electrolyte feeding during open-circuit holds	HFR stable over 800 h vs. 0.10 → 0.23 Ω cm^2 rise under dry open-circuit holds; single cell [26,27,50]	Stack-level shunt-current, RC trade-off not yet quantified
System-level	Sacrificial-metal cathode protection (Pb, Zn, Sn, Al)	Reverse-current stability factor 73 → 97–100%; AEL [49]	AEMEL transfer not yet demonstrated; possible electrolyte contamination
System-level	Energy-storage buffering (PV–battery–electrolyzer)	Stable ~0.45 A output from intermittent PV input over 12 h [76], proof-of-concept	AEMEL-specific durability gain not quantified; capital cost vs. lifetime benefits unresolved
Materials	Zirconia reinforcement (mechanical, not durability)	Impact strength +57%, crossover 0.075 → 0.033 mA cm^{-2}; but drift 0.15 → 1.65 μV $cycle^{-1}$ over 11,000 cycles; single cell [12]	Drift penalty not tested under a true stop
Materials	Carbon-encapsulated Ni_3Mo cathode ($Ni_3Mo@C60$)	0.73 mV $cycle^{-1}$ over 192 open-circuit cycles (encapsulated) vs. 6.7 mV $cycle^{-1}$ over 48 cycles (bare), a 9-fold reduction [9]	Tested over hundreds rather than thousands of cycles
Materials	Pt/C cathode under reverse current	ΔE_cell +0.05 V vs. +1.7 V for NiMo/C at 1.5 A cm^{-2}, after 30 min polarity inversion at 0.03 A cm^{-2} [13]	PGM dependence; conflicts with PGM-free AEMEL design objectives

No single intervention addresses the full range of failure modes, so a practical durability strategy combines levers from all three categories. The current AEMEL literature lacks a single demonstration that integrates levers across all three layers under a realistic intermittent test protocol, which is the gap future durability studies should address.

7. Knowledge Gaps and Research Needs

Durability data for AEMEL under intermittent operation cannot yet be compared quantitatively between laboratories, which limits how far reported rates can be generalized [74,80]. Five gaps follow from the evidence reviewed above, each stated as what the present evidence establishes, what limits it, and what measurement would close it.

1. Severity of a stop has no shared metric. Per-cycle rates span more than four orders of magnitude, and protocol rather than material accounts for most of that range (Sections 5.2.3 and 5.3). The parameters that set severity are rarely reported within a uniform taxonomy [8,14,55,81], so a protocol label alone does not make two rates comparable. Severity should instead be reported as a vector—minimum cell voltage, peak reverse current, reverse charge, voltage decay rate, and dwell times at open circuit and at low voltage—together with the thermal and hydraulic state of the hold. One component of that vector is itself unresolved: whether the irreversible ohmic penalty of a dry hold reflects dehydration or cation loss at low hydration (Section 6.1). The two are coupled, since lost cations lower water uptake [73]; ion-exchange capacity measured after full rehydration would separate them [25].
2. Electrode-resolved evidence is confined to single cells and one anode chemistry. Three AEMEL single-cell studies have decoupled the electrode potentials under open-circuit or reverse-current stressors, and all place the loss at the cathode (Section 5.2.2). All three compared cathode catalysts against a fixed NiFe-LDH anode in KOH, so their stable anode belongs to that pairing; in pure-water-fed cells, anode restructuring and ionomer oxidation dominated even under steady load [24,82]. The pseudo-reference used under forced inversion is reliable only up to 0.2 A cm^{-2}, and no reference electrode has been used in a stack, where shunt currents and cell-to-cell imbalance complicate the potential reference; scale-up itself has been tested only under steady load, as in a 63.6 cm^2 cell run for 2000 h [83]. Repeating these protocols with the anode varied as well as the cathode, and in multi-cell hardware with the discharge path and thermal state reported, is the outstanding validation step. Materials screening carries the same limitation: half-cell screening does not predict durability in the electrolyzer [84], and a cathode that degraded only slightly under steady load failed within tens of open-circuit stops [9]; durability studies should report per-cycle voltage rise against a stated severity vector over more than 1000 h of intermittent operation [85].
3. Electrical events and materials changes are rarely observed on the same cell. A reference electrode assigns a loss to one electrode, online dissolved-metal detection shows when metal leaves it, and operando spectroscopy ties a potential excursion to a specific phase transition (Section 4). Few AEMEL studies have combined even two of these on one cell, so the fraction of reverse current arising from dissolved gas rather than from electrode-surface redox remains unquantified, and dissolution cannot be attributed to a particular stressor within a protocol. Pairing any two under a single intermittent protocol would close the gap.
4. The protocols do not reproduce field operation. Section 3.2 sets out what synthetic waveforms omit: stochastic event intervals, co-varying temperature, pressure and flow, service-lifetime cycle counts, and stack-level flow paths. Closing this requires

durability testing under measured renewable traces with the thermal and hydraulic state allowed to co-vary. Pure-water feed, one of the modes that distinguishes AEMEL (Section 2.2), has not been tested under a true open-circuit stop [51], although a baseline pure-water cell degraded at 0.67 mV h^{-1} even under steady load [86]; the electrolyte-concentration lever of Section 6.1 is unavailable there. Gas purity is the most readily addressable case: no AEMEL study has logged the hydrogen-in-oxygen fraction continuously through a shutdown and restart, although the in-line sensing already exists on at least one stack (Section 6.2).

5. No AEMEL-specific techno-economic assessment of intermittent duty exists [87]. Published PEMEL and AEL assessments show that intermittent coupling erodes project economics through reduced capacity factor and accelerated per-cycle degradation, curtailing stack life below commercial targets [16,18]; the calculation in Section 5.2.3 indicates the scale of what is at stake. Those assessments do not transfer, because non-PGM catalysts shift the cost balance away from catalyst replacement toward the membrane and balance of plant [88,89], and the dominant failure modes are specific to the cathode catalyst chemistry [90]. An AEMEL-specific assessment should be built on per-cycle degradation rates measured under a defined stop protocol rather than extrapolated from steady operation.

8. Conclusions

The evidence assembled here supports one organizing claim: shutdown transients and open-circuit holds, and not only steady high-load operation or load cycling, are a major and underappreciated degradation pathway in renewable-coupled AEMEL. Under that stressor class the loss concentrates at the cathode in the three single-cell studies that have resolved the two electrodes, all with a NiFe-LDH anode, and its severity scales with the stability of the cathode metal, leaving Mo-containing non-precious HER catalysts the most exposed and Pt-based cathodes comparatively tolerant. Severity is governed by the conditions imposed at the stop rather than by intermittency as such, which makes the boundary conditions of a shutdown a design variable on the same footing as catalyst choice. The evidence base behind these conclusions remains small, dominated by single cells and obtained almost entirely under synthetic waveforms, and its electrode localization comes from studies that varied only the cathode; it establishes mechanism and ranks severity between protocols without yet supporting lifetime prediction under field conditions. Mitigation effort belongs at the stop and, for the cells tested, at the hydrogen electrode; the measurements that would place it on firmer evidence are set out in Section 7.

Supplementary Materials: The following supporting information can be downloaded at: https://www.mdpi.com/article/10.3390/hydrogen7040195/s1. Table S1: Intermittent, shutdown and reverse-current protocols reported in the liquid alkaline water electrolysis (AEL) studies cited in this review.

Author Contributions: Conceptualization, M.M.R. and M.S.; methodology, M.M.R.; formal analysis, M.M.R.; investigation, M.M.R.; data curation, M.M.R.; writing—original draft preparation, M.M.R.; writing—review and editing, M.M.R. and M.S.; visualization, M.M.R.; supervision, M.S.; project administration, M.S.; funding acquisition, M.S. All authors have read and agreed to the published version of the manuscript.

Funding: M.M.R. is supported by a doctoral scholarship within the National PhD Programme in Materials, Sustainable Processes and Systems for Energy Transition at Politecnico di Torino, financed by the Italian Ministry of University and Research (MUR) under the project

"iENTRANCE@ENL—Infrastructure for Energy Transition and Circular Economy@EuroNanoLab", CUP B33C22000710006.

Institutional Review Board Statement: Not applicable.

Informed Consent Statement: Not applicable.

Data Availability Statement: No new experimental data were created in this study. The quantitative values plotted in Figures 6 and 7 were digitized from figures published in the cited source studies; the digitized datasets are available from the corresponding author on request, subject to the licensing terms of the original publications.

Acknowledgments: The authors gratefully acknowledge the Department of Energy (DENERG), Politecnico di Torino, for institutional and technical support. During the preparation of this manuscript, the authors used Claude (OPUS 5 model) for language editing and consistency checking. The authors have reviewed and edited the output and take full responsibility for the content of this publication.

Conflicts of Interest: The authors declare no conflicts of interest.

Abbreviations

The following abbreviations are used in this manuscript:

ADT	accelerated durability test
AEL	alkaline electrolyzer/alkaline water electrolysis
AEM	anion exchange membrane
AEMEL	anion exchange membrane water electrolyzer
AEMWE	anion exchange membrane water electrolysis
AWE	alkaline water electrolysis
BoP	balance of plant
BOT	beginning of test
CC	constant current
CP	chronopotentiometry
CV	cyclic voltammetry
DI	deionized (water)
DRT	distribution of relaxation times
ECSA	electrochemically active surface area
EDX/EDS	energy-dispersive X-ray spectroscopy
EIS	electrochemical impedance spectroscopy
EOT	end of test
FESEM	field-emission scanning electron microscopy
FIB	focused ion beam
GC	gas chromatography
GDL	gas diffusion layer
HER	hydrogen evolution reaction
HFR	high-frequency resistance
ICP-MS	inductively coupled plasma mass spectrometry
ICP-OES	inductively coupled plasma optical emission spectrometry
IEA	International Energy Agency
LAEL	liquid alkaline electrolyzer
LAWE	liquid alkaline water electrolysis
LCOH	levelized cost of hydrogen
LSV	linear sweep voltammetry
MEA	membrane electrode assembly
OCP	open-circuit potential
OCV	open-circuit voltage
OER	oxygen evolution reaction
PEM	proton exchange membrane

PEMEL	proton exchange membrane water electrolyzer
PEMWE	proton exchange membrane water electrolysis
PGM	platinum group metal
PTL	porous transport layer
PtX	power-to-X
PV	photovoltaic
RC	reverse current
RDE	rotating disk electrode
RHE	reversible hydrogen electrode
SEM	scanning electron microscopy
SERS	surface-enhanced Raman spectroscopy
TEA	techno-economic analysis
TEM	transmission electron microscopy
ToF-SIMS	time-of-flight secondary ion mass spectrometry
VRE	variable renewable energy
XPS	X-ray photoelectron spectroscopy
XRD	X-ray diffraction

References

1. Ferriday, T.B.; Sampathkumar, S.N.; Middleton, P.H.; Kolhe, M.L.; Van Herle, J. A Review of Membrane Electrode Assemblies for the Anion Exchange Membrane Water Electrolyser: Perspective on Activity and Stability. *Int. J. Energy Res.* **2024**, *2024*. https://doi.org/10.1155/2024/7856850.
2. International Energy Agency. *Renewables 2025*; International Energy Agency: Paris, France, 2025; p. 147.
3. International Energy Agency. *Global Hydrogen Review 2025*; International Energy Agency: Paris, France, 2025; pp. 79–81, 100, 108.
4. International Energy Agency. *The Future of Hydrogen: Seizing Today's Opportunities*; International Energy Agency: Paris, France, 2019; pp. 17, 37.
5. Martinez Lopez, V.A.; Ziar, H.; Haverkort, J.W.; Zeman, M.; Isabella, O. Dynamic Operation of Water Electrolyzers: A Review for Applications in Photovoltaic Systems Integration. *Renew. Sustain. Energy Rev.* **2023**, *182*, 113407. https://doi.org/10.1016/j.rser.2023.113407.
6. Marquez, R.A.; Bender, J.T.; Aleman, A.M.; Kalokowski, E.; Vy Le, T.; Williamson, C.L.; Frederiksen, M.L.; Kawashima, K.; Chukwuneke, C.E.; Dolocan, A.; et al. Insights into Catalyst Degradation during Alkaline Water Electrolysis under Variable Operation. *Energy Environ. Sci.* **2025**, *18*, 7170–7187. https://doi.org/10.1039/D5EE02194D.
7. Gladik, A.; Riedel, M.; Eichel, R.A. Anion Exchange Membrane Electrolysis at Work—Investigating Impact of Starting Parameters and Start–Stop Operation on Cold Start Behavior and Degradation. *J. Power Sources* **2025**, *628*, 235878. https://doi.org/10.1016/j.jpowsour.2024.235878.
8. Gladik, A.; Riedel, M.; Eichel, R.A. Intermittent Operation of an Anion Exchange Membrane Electrolysis System—Unraveling Shutdowns as an Underestimated Risk for Degradation. *Int. J. Hydrogen Energy* **2025**, *165*, 150793. https://doi.org/10.1016/j.ijhydene.2025.150793.
9. Jeon, S.S.; Choi, Y.; Lee, J.W.; Haaring, R.; Lee, W.; Jeon, H.; Nam, J.; Lee, E.; Lee, S.; Kim, M.; et al. Degradation of NiMo Catalyst Under Intermittent Operation of Anion Exchange Membrane Water Electrolyzer and Its Mitigation by Carbon Encapsulation. *Adv. Energy Mater.* **2025**, *15*, 2501800. https://doi.org/10.1002/aenm.202501800.
10. Galkina, I.; Faid, A.Y.; Jiang, W.; Scheepers, F.; Borowski, P.; Sunde, S.; Shviro, M.; Lehnert, W.; Mechler, A.K. Stability of Ni–Fe-Layered Double Hydroxide Under Long-Term Operation in AEM Water Electrolysis. *Small* **2024**, *20*, 2311047. https://doi.org/10.1002/smll.202311047.
11. Nam, J.; Jeon, S.S.; Lee, W.; Choi, Y.; Jeon, H.; Lee, H. Load Fluctuation-Induced Degradation of Pt-Based Alloy Catalysts in anion Exchange Membrane Water Electrolyzers. *Chem. Eng. J.* **2025**, *523*, 168371. https://doi.org/10.1016/j.cej.2025.168371.
12. Motealleh, B.; Liu, Z.; Masel, R.I.; Sculley, J.P.; Richard Ni, Z.; Meroueh, L. Next-Generation Anion Exchange Membrane Water Electrolyzers Operating for Commercially Relevant Lifetimes. *Int. J. Hydrogen Energy* **2021**, *46*, 3379–3386. https://doi.org/10.1016/j.ijhydene.2020.10.244.
13. Guruprasad, N.; van der Schaaf, J.; de Groot, M.T. Unraveling the Impact of Reverse Currents on Electrode Stability in Anion Exchange Membrane Water Electrolysis. *J. Power Sources* **2024**, *613*, 234877. https://doi.org/10.1016/j.jpowsour.2024.234877.
14. Wan, Z.; Rui, D.; Wu, L.; Liu, G.; Li, J.; Du, X. Durability of NiFe-Based Oxygen Evolution Electrocatalysts in AEM Water Electrolyzer under Fluctuating Power Supply. *J. Colloid Interface Sci.* **2025**, *688*, 456–468. https://doi.org/10.1016/j.jcis.2025.02.135.

15. Ursúa, A.; Barrios, E.L.; Pascual, J.; San Martín, I.; Sanchis, P. Integration of Commercial Alkaline Water Electrolysers with Renewable Energies: Limitations and Improvements. *Int. J. Hydrogen Energy* **2016**, *41*, 12852–12861. https://doi.org/10.1016/j.ijhydene.2016.06.071.
16. Berrada, A.; Sanjari, M.J.; El Mrabet, R. Techno-Economic Assessment of Hydrogen Production: Comparative Analysis of Electrolyser Technologies in a Hybrid PV/Wind System. *Int. J. Hydrogen Energy* **2025**, *141*, 193–211. https://doi.org/10.1016/j.ijhydene.2025.05.384.
17. Pellegrino, A.; Potgieter, M.; Tedesco, M.; Tamburini, A.; Creus, J. Experimental Investigation and Techno-Economic Assessment on Anion Exchange Membrane Electrolyser with Different Cell Components. *Int. J. Hydrogen Energy* **2025**, *184*, 151894. https://doi.org/10.1016/j.ijhydene.2025.151894.
18. Aminaho, E.N.; Aminaho, N.S.; Aminaho, F. Techno-Economic Assessments of Electrolyzers for Hydrogen Production. *Appl. Energy* **2025**, *399*, 126515. https://doi.org/10.1016/j.apenergy.2025.126515.
19. Vinodh, R.; Kalanur, S.S.; Natarajan, S.K.; Pollet, B.G. Recent Advancements of Polymeric Membranes in Anion Exchange Membrane Water Electrolyzer (AEMWE): A Critical Review. *Polymers* **2023**, *15*, 2144. https://doi.org/10.3390/polym15092144.
20. Ng, W.; Wong, W.; Rosli, N.; Loh, K. Commercial Anion Exchange Membranes (AEMs) for Fuel Cell and Water Electrolyzer Applications: Performance, Durability, and Materials Advancement. *Separations* **2023**, *10*, 424. https://doi.org/10.3390/separations10080424.
21. Mustapha, F.; Guilbert, D.; Gross, B. Advancements in Anion Exchange Membrane Electrolysers: From Catalysts to Life Cycle Assessment. *Int. J. Sustain. Energy* **2025**, *44*, 2520812. https://doi.org/10.1080/14786451.2025.2520812.
22. Volk, E.K.; Kreider, M.E.; Kwon, S.; Alia, S.M. Recent Progress in Understanding the Catalyst Layer in Anion Exchange Membrane Electrolyzers—Durability, Utilization, and Integration. *EES Catal.* **2024**, *2*, 109–137. https://doi.org/10.1039/D3EY00193H.
23. Lei, J.; Wang, Z.; Zhang, Y.; Ju, M.; Fei, H.; Wang, S.; Fu, C.; Yuan, X.; Fu, Q.; Farid, M.U.; et al. Understanding and Resolving the Heterogeneous Degradation of Anion Exchange Membrane Water Electrolysis for Large-Scale Hydrogen Production. *Carbon Neutrality* **2024**, *3*, 25. https://doi.org/10.1007/s43979-024-00101-y.
24. Muhyuddin, M.; Santoro, C.; Osmieri, L.; Ficca, V.C.A.; Friedman, A.; Yassin, K.; Pagot, G.; Negro, E.; Konovalova, A.; Lindquist, G.; et al. Anion-Exchange-Membrane Electrolysis with Alkali-Free Water Feed. *Chem. Rev.* **2025**, *125*, 6906–6976. https://doi.org/10.1021/acs.chemrev.4c00466.
25. Altinisik, H.; Celebi, C.; Ozden, A.; Devrim, Y.; Ozgur Colpan, C. A Review on Membranes for Anion Exchange Membrane Water Electrolyzers. *Renew. Sustain. Energy Rev.* **2026**, *226*, 116277. https://doi.org/10.1016/j.rser.2025.116277.
26. Niaz, A.K.; Lee, W.; Yang, S.; Lim, H.-T. Tracing Resistances of Anion Exchange Membrane Water Electrolyzer during Long-Term Stability Tests. *J. Electrochem. Sci. Technol.* **2021**, *12*, 358–364. https://doi.org/10.33961/jecst.2021.00094.
27. Niaz, A.K.; Akhtar, A.; Park, J.-Y.; Lim, H.-T. Effects of the Operation Mode on the Degradation Behavior of Anion Exchange Membrane Water Electrolyzers. *J. Power Sources* **2021**, *481*, 229093. https://doi.org/10.1016/j.jpowsour.2020.229093.
28. Narayanaru, S.; Miyanishi, S.; Kuroki, H.; Anilkumar, G.M.; Yamaguchi, T. Start-Stop Cyclic Durability Analysis of Membrane-Electrode Assemblies Using Polyflourene-Based Electrolytes for an Anion-Exchange Membrane Water Electrolyzer. *ACS Sustain. Chem. Eng.* **2023**, *11*, 9295–9302. https://doi.org/10.1021/acssuschemeng.2c07387.
29. Lim, K.L.; Wong, C.Y.; Wong, W.Y.; Loh, K.S.; Selambakkannu, S.; Othman, N.A.F.; Yang, H. Radiation-Grafted Anion-Exchange Membrane for Fuel Cell and Electrolyzer Applications: A Mini Review. *Membranes* **2021**, *11*, 397. https://doi.org/10.3390/membranes11060397.
30. Li, C.; Baek, J.-B. The Promise of Hydrogen Production from Alkaline Anion Exchange Membrane Electrolyzers. *Nano Energy* **2021**, *87*, 106162. https://doi.org/10.1016/j.nanoen.2021.106162.
31. Ursúa, A.; San Martín, I.; Barrios, E.L.; Sanchis, P. Stand-Alone Operation of an Alkaline Water Electrolyser Fed by Wind and Photovoltaic Systems. *Int. J. Hydrogen Energy* **2013**, *38*, 14952–14967. https://doi.org/10.1016/j.ijhydene.2013.09.085.
32. Hassan, A.; Abdel-Rahim, O.; Bajaj, M.; Zaitsev, I. Power Electronics for Green Hydrogen Generation with Focus on Methods, Topologies, and Comparative Analysis. *Sci. Rep.* **2024**, *14*, 24767. https://doi.org/10.1038/s41598-024-76191-6.
33. Buttler, A.; Spliethoff, H. Current Status of Water Electrolysis for Energy Storage, Grid Balancing and Sector Coupling via Power-to-Gas and Power-to-Liquids: A Review. *Renew. Sustain. Energy Rev.* **2018**, *82*, 2440–2454. https://doi.org/10.1016/j.rser.2017.09.003.
34. Li, D.; Motz, A.R.; Bae, C.; Fujimoto, C.; Yang, G.; Zhang, F.-Y.; Ayers, K.E.; Kim, Y.S. Durability of Anion Exchange Membrane Water Electrolyzers. *Energy Environ. Sci.* **2021**, *14*, 3393–3419. https://doi.org/10.1039/D0EE04086J.
35. Du, N.; Roy, C.; Peach, R.; Turnbull, M.; Thiele, S.; Bock, C. Anion-Exchange Membrane Water Electrolyzers. *Chem. Rev.* **2022**, *122*, 11830–11895.
36. Yang, Y.; Li, P.; Zheng, X.; Sun, W.; Dou, S.X.; Ma, T.; Pan, H. Anion-Exchange Membrane Water Electrolyzers and Fuel Cells. *Chem. Soc. Rev.* **2022**, *51*, 9620–9693. https://doi.org/10.1039/D2CS00038E.

37. Miller, H.A.; Bouzek, K.; Hnat, J.; Loos, S.; Bernäcker, C.I.; Weißgärber, T.; Röntzsch, L.; Meier-Haack, J. Green Hydrogen from Anion Exchange Membrane Water Electrolysis: A Review of Recent Developments in Critical Materials and Operating Conditions. *Sustain. Energy Fuels* **2020**, *4*, 2114–2133.
38. Ferriday, T.B.; Middleton, P.H.; Kolhe, M.L.; Van Herle, J. Raising the Temperature on Electrodes for Anion Exchange Membrane Electrolysis—Activity and Stability Aspects. *Chem. Eng. J. Adv.* **2023**, *16*, 100525. https://doi.org/10.1016/j.ceja.2023.100525.
39. Cai, J.; Weng, C.; Zhang, R.; Li, Q.; Zhang, T.; Shi, Z. Comparative Analysis on the Dynamic Operation Performance of photovoltaic/Thermal Powered Proton Exchange Membrane Water Electrolysis System (PV/T-PEMWE) under Different Connection Modes. *Renew. Energy* **2023**, *219*, 119566. https://doi.org/10.1016/j.renene.2023.119566.
40. Razmjooei, F.; Morawietz, T.; Taghizadeh, E.; Hadjixenophontos, E.; Mues, L.; Gerle, M.; Wood, B.D.; Harms, C.; Gago, A.S.; Ansar, S.A.; et al. Increasing the Performance of an Anion-Exchange Membrane Electrolyzer Operating in Pure Water with a Nickel-Based Microporous Layer. *Joule* **2021**, *5*, 1776–1799. https://doi.org/10.1016/j.joule.2021.05.006.
41. Yanagi, R.; Yang, P.; Tricker, A.W.; Chen, Y.; Scott, M.C.; Berlinger, S.A.; Zenyuk, I.V.; Peng, X. Enhancing Water and Oxygen Transport through Electrode Engineering for AEM Water Electrolyzers. *Joule* **2025**, *9*, 102001. https://doi.org/10.1016/j.joule.2025.102001.
42. Xu, Q.; Zhang, L.; Zhang, J.; Wang, J.; Hu, Y.; Jiang, H.; Li, C. Anion Exchange Membrane Water Electrolyzer: Electrode Design, Lab-Scaled Testing System and Performance Evaluation. *EnergyChem* **2022**, *4*, 100087.
43. Ursúa, A.; Martín, S.; Sanchis, P. Design of a Programmable Power Supply to Study the Performance of an Alkaline Electrolyser under Different Operating Conditions. In Proceedings of the 2012 IEEE International Energy Conference and Exhibition (Energycon), Florence, Italy, 9–12 September 2012; pp. 259–264. https://doi.org/10.1109/energycon.2012.6347763.
44. Caponi, R.; Vizza, D.; Bassano, C.; Del Zotto, L.; Bocci, E. Dynamic Comparative Assessment of Long-Term Simulation Strategies for an Off-Grid PV–AEM Electrolyzer System. *Energies* **2025**, *18*, 4209. https://doi.org/10.3390/en18154209.
45. Ursúa, A.; Gandía, L.; Sanchis, P. Hydrogen Production from Water Electrolysis: Current Status and Future Trends. *Proc. IEEE* **2012**, *100*, 410–426. https://doi.org/10.1109/jproc.2011.2156750.
46. Ul Hassan, N.; Volk, E.K.; Kreider, M.; Dinh, H.N.; Pivovar, B.S.; Alia, S.M. Anion Exchange Membrane Water Electrolyzer Accelerated Durability Assessment Using Potential Cycling. *ECS Meet. Abstr.* **2024**, *MA2024-02*, 3172. https://doi.org/10.1149/ma2024-02453172mtgabs.
47. Shaik, S.; Kim, J.; Kabiraz, M.K.; Aziz, F.; Park, J.Y.; Anne, B.R.; Li, M.; Huang, H.; Nam, K.M.; Jo, D.; et al. Rapid Outgassing of Hydrophilic TiO_2 Electrodes Achieves Long-Term Stability of Anion Exchange Membrane Water Electrolyzers. *Nanomicro Lett.* **2025**, *17*, 186. https://doi.org/10.1007/s40820-025-01696-2.
48. Kuang, W.; Cui, Z.; Wang, C.; Chen, T.; Wang, Q.; Li, S.; Yang, T.; Liu, J. Self-Supported Ni/$Ni(OH)_2$ Electrodes for High-Performance Alkaline and AEM Water Electrolysis. *Adv. Energy Mater.* **2025**, *15*, 2406080. https://doi.org/10.1002/aenm.202406080.
49. Kim, Y.; Jung, S.M.; Kim, K.S.; Kim, H.Y.; Kwon, J.; Lee, J.; Cho, H.S.; Kim, Y.T. Cathodic Protection System against a Reverse-Current after Shut-Down in Zero-Gap Alkaline Water Electrolysis. *JACS Au* **2022**, *2*, 2491–2500. https://doi.org/10.1021/jacsau.2c00314.
50. Niaz, A.K.; Lim, H.-T. Stability Tests on Anion Exchange Membrane Water Electrolyzer under On-Off Cycling with Continuous Solution Feeding. *J. Electrochem. Sci. Technol.* **2022**, *13*, 369–376. https://doi.org/10.33961/jecst.2022.00241.
51. Yassin, K.; Baranov, A.A.; Zhong, J.; Dekel, D.R. High-Temperature Anion Exchange Membrane Water Electrolysis. *ACS Energy Lett.* **2026**, *11*, 2257–2264. https://doi.org/10.1021/acsenergylett.5c04187.
52. Malek, A.; Wu, L.; Li, Y.; Li, C.; Chen Yuhao and Hazazi, K.; Xue, Y.; Lu, X. Transient-Promoter-Stabilized NiFe Oxyhydroxide Enables Durable kW-Scale Water Splitting Under Fluctuating Power. *Angew. Chem.-Int. Ed.* **2025**, *65*, e20825. https://doi.org/10.1002/anie.202520825.
53. Campagna Zignani, S.; Faro, M.L.; Carbone, A.; Italiano, C.; Trocino, S.; Monforte, G.; Aricò, A.S. Performance and Stability of a Critical Raw Materials-Free Anion Exchange Membrane Electrolysis Cell. *Electrochim. Acta* **2022**, *413*, 140078. https://doi.org/10.1016/j.electacta.2022.140078.
54. Rahman, M.M. Effect of Wind Power Profile on the Degradation of Proton Exchange Membrane Water Electrolyzer. Master's Thesis, University of Science and Technology (UST), Daejeon, Republic of Korea, 2022.
55. Abdel Haleem, A.; Huyan, J.; Nagasawa, K.; Kuroda, Y.; Nishiki, Y.; Kato, A.; Nakai, T.; Araki, T.; Mitsushima, S. Effects of Operation and Shutdown Parameters and Electrode Materials on the Reverse Current Phenomenon in Alkaline Water Analyzers. *J. Power Sources* **2022**, *535*, 231454. https://doi.org/10.1016/j.jpowsour.2022.231454.
56. Oda, K.; Kuroda, Y.; Mitsushima, S. Investigation of Charge–Discharging Behavior of Metal Oxide–Based Anode Electrocatalysts for Alkaline Water Electrolysis to Suppress Degradation Due to Reverse Current. *Electrocatalysis* **2023**, *14*, 499–510. https://doi.org/10.1007/s12678-023-00815-0.

57. Koch, S.; Disch, J.; Kilian, S.K.; Han, Y.; Metzler, L.; Tengattini, A.; Helfen, L.; Schulz, M.; Breitwieser, M.; Vierrath, S. Water Management in Anion-Exchange Membrane Water Electrolyzers under Dry Cathode Operation. *RSC Adv.* **2022**, *12*, 20778–20784. https://doi.org/10.1039/D2RA03846C.
58. Mar, H.; Mardle, P.; Tsay, K.; Xie, Z.; Kodra, O.; Qu, W.; Wang, G. Edge-Type Reference Electrode Application for AEM-WE Durability Testing. *J. Electrochem. Soc.* **2025**, *172*, 044510. https://doi.org/10.1149/1945-7111/adc8d6.
59. Ranz, M.; Grabner, B.; Schweighofer, B.; Wegleiter, H.; Trattner, A. Deciphering Anion Exchange Membrane Water Electrolysis: A Distribution of Relaxation Times Approach. *ECS Trans.* **2024**, *114*, 483–492. https://doi.org/10.1149/11405.0483ecst.
60. Ranz, M.; Grabner, B.; Schweighofer, B.; Wegleiter, H.; Trattner, A. Dynamics of Anion Exchange Membrane Electrolysis: Unravelling Loss Mechanisms with Electrochemical Impedance Spectroscopy, Reference Electrodes and Distribution of Relaxation Times. *J. Power Sources* **2024**, *605*, 234455. https://doi.org/10.1016/j.jpowsour.2024.234455.
61. Fang, Y.; Shen, J.; Deng, L.; Zhang, Y.; Feng, C.; Zuo, J.; Li, J.; Zheng, J.P.; Zhang, C.; Jin, L. Validated Distribution of Relaxation Times Mapping of Decoupled Polarization Mechanisms in Anion Exchange Membrane Electrolyzers. *Adv. Sustain. Syst.* **2026**, *10*, e70411. https://doi.org/10.1002/adsu.70411.
62. Nuggehalli Sampathkumar, S.; Ferriday, T.B.; Daviran, S.; Moussaoui, H.; Aubin, P.; Lawand, K.; Mensi, M.; Schouwink, P.A.; Taureg, A.; Subotić, V.; et al. Combinatorial Use of Reference Electrodes and DRT for Disentangling AEM Electrolyzer Losses. *Energy and Fuels* **2025**, *39*, 16485–16500. https://doi.org/10.1021/acs.energyfuels.5c01799.
63. Uchino, Y.; Kobayashi, T.; Hasegawa, S.; Nagashima, I.; Sunada, Y.; Manabe, A.; Nishiki, Y.; Mitsushima, S. Dependence of the Reverse Current on the Surface of Electrode Placed on a Bipolar Plate in an Alkaline Water Electrolyzer. *Electrochemistry* **2018**, *86*, 138–144. https://doi.org/10.5796/electrochemistry.17-00102.
64. Tricker, A.W.; Lee, J.K.; Shin, J.R.; Danilovic, N.; Weber, A.Z.; Peng, X. Design and Operating Principles for High-Performing Anion Exchange Membrane Water Electrolyzers. J. Power Sources 2023, 567, 232967. https://doi.org/10.1016/j.jpowsour.2023.232967.
65. Holmin, S.; Näslund, L.Å.; Ingason, Á.S.; Rosen, J.; Zimmerman, E. Corrosion of Ruthenium Dioxide Based Cathodes in Alkaline Medium Caused by Reverse Currents. *Electrochim. Acta* **2014**, *146*, 30–36. https://doi.org/10.1016/j.electacta.2014.09.024.
66. Mayerhöfer, B.; Speck, F.D.; Hegelheimer, M.; Bierling, M.; Abbas, D.; McLaughlin, D.; Cherevko, S.; Thiele, S.; Peach, R. Electrochemical- and Mechanical Stability of Catalyst Layers in Anion Exchange Membrane Water Electrolysis. *Int. J. Hydrogen Energy* **2022**, *47*, 4304–4314. https://doi.org/10.1016/j.ijhydene.2021.11.083.
67. Wang, Z.; Wang, Y.; Py, B.; Maradesa, A.; Liu, J.; Wan, T.H.; Saccoccio, M.; Ciucci, F. DRTtools: Freely Accessible Distribution of Relaxation Times Analysis for Electrochemical Impedance Spectroscopy. *ACS Electrochemistry* **2025**, *1*, 2680–2689. https://doi.org/10.1021/acselectrochem.5c00334.
68. Ferrero, D.; Mansourkiaei, M.; Trapani, D.; Consoli, D.; Prevedello, P.; Assenza, I.; Matter, P.; Hery, T.; Fox, M.; Monteverde, A.; et al. Performance Evaluation and Durability Assessment of Hybrid Alkaline/Membrane Electrolysis Cell Designs. *J. Power Sources* **2025**, *658*, 238239. https://doi.org/10.1016/j.jpowsour.2025.238239.
69. Wang, Z.; Zheng, Y.R.; Montoya, J.; Hochfilzer, D.; Cao, A.; Kibsgaard, J.; Chorkendorff, I.; Nørskov, J.K. Origins of the Instability of Nonprecious Hydrogen Evolution Reaction Catalysts at Open-Circuit Potential. *ACS Energy Lett.* **2021**, *6*, 2268–2274. https://doi.org/10.1021/acsenergylett.1c00876.
70. Esfandiari, N.; Aliofkhazraei, M.; Colli, A.N.; Walsh, F.C.; Cherevko, S.; Kibler, L.A.; Elnagar, M.M.; Lund, P.D.; Zhang, D.; Omanovic, S.; et al. Metal-Based Cathodes for Hydrogen Production by Alkaline Water Electrolysis: Review of Materials, Degradation Mechanism, and Durability Tests. *Prog. Mater. Sci.* **2024**, *144*, 101254.
71. Clean Hydrogen Joint Undertaking. *Strategic Research and Innovation Agenda 2021–2027*; Clean Hydrogen Joint Undertaking: Brussels, Belgium, 2022.
72. Kuhnert, E.; Mayer, K.; Heidinger, M.; Rienessel, C.; Hacker, V.; Bodner, M. Impact of Intermittent Operation on Photovoltaic-PEM Electrolyzer Systems: A Degradation Study Based on Accelerated Stress Testing. *Int. J. Hydrogen Energy* **2024**, *55*, 683–695. https://doi.org/10.1016/j.ijhydene.2023.11.249.
73. Erimban, S.; Bombau, I.J.; Karnes, J.J.; Molinero, V. Degradation of Anion Exchange Membranes by Cation Elimination: Impact on Water Uptake, Nanostructure, and Ionic Mobility. *J. Phys. Chem. C* **2024**, *128*, 11033–11045. https://doi.org/10.1021/acs.jpcc.4c02639.
74. Rodríguez, V.; Gómez-Sacedón, C.; Sánchez, P.; de Lucas-Consuegra, A. Anion Exchange Membrane Electrolysis beyond the Lab Scale: A Review on Research and Industry Stacks. *Curr. Opin. Chem. Eng.* **2026**, *51*, 101218.
75. Schofield, L.; Paren, B.; Macdonald, R.; Shao-Horn, Y.; Mallapragada, D. Dynamic Optimization of Proton Exchange Membrane Water Electrolyzers Considering Usage-Based Degradation. AIChE J. 2025, 71, e18635. https://doi.org/10.1002/aic.18635.
76. Sun, Z.; Wang, G.; Koh, S.W.; Ge, J.; Zhao, H.; Hong, W.; Fei, J.; Zhao, Y.; Gao, P.; Miao, H.; et al. Solar-Driven Alkaline Water Electrolysis with Multifunctional Catalysts. *Adv. Funct. Mater.* **2020**, *30*, 2002138. https://doi.org/10.1002/adfm.202002138.

77. Ranz, M.; Grabner, B.; Schweighofer, B.; Wegleiter, H.; Trattner, A. Degradation in Anion Exchange Membrane Water Electrolysis: Insights from a Distribution of Relaxation Times Approach. *J. Electrochem. Soc.* **2025**, *172*, 104508. https://doi.org/10.1149/1945-7111/ae0dbb.
78. Cong, L.; Tang, C.; Li, X.; He, W.; Wang, C.; Angelica, E.; Zhang, Q. Li-Doping and Pyrolysis Engineered Robust Anode for Intermittency-Resilient AEM Electrolysis. *Adv. Energy Mater.* **2025**, *15*, e04707. https://doi.org/10.1002/aenm.202504707.
79. Dong, A.; Lin, G.; Li, Z.; Wu, W.; Cao, X.; Li, W.; Wang, L.; Zhao, Y.; Chen, D.; Sun, L. Interlayer-Bonded Ni/MoO_2 Electrocatalyst for Efficient Hydrogen Evolution Reaction with Stability over 6000 h at 1000 mA cm^{-2}. *Nat. Commun.* **2025**, *16*, 4955. https://doi.org/10.1038/s41467-025-59933-6.
80. Amirsalehi, M.; Mosali, V.S.S.; Al-Murisi, M.; Bashiri, S.; Gopi, H.; Satjaritanun, P.; Britton, B.; Swider-Lyons, K.; Mustain, W.E. Beyond Catalysts and Membranes: Using Cell Assembly and Operating Strategies to Significantly Improve the Performance of AEM Electrolyzers. *J. Electrochem. Soc.* **2026**, *173*, 054502. https://doi.org/10.1149/1945-7111/ae4929.
81. Nguyen, E.; Olivier, P.; Péra, M.-C.; Pahon, E.; Roche, R.; Lefranc, O.; Claudel, F. Impact of Short-Term Intermittent Operation on Experimental Industrial PEM and Alkaline Electrolyzers. *Int. J. Hydrogen Energy* **2025**, *126*, 516–530. https://doi.org/10.1016/j.ijhydene.2025.04.129.
82. Krivina, R.A.; Lindquist, G.A.; Beaudoin, S.R.; Stovall, T.N.; Thompson, W.L.; Twight, L.P.; Marsh, D.; Grzyb, J.; Fabrizio, K.; Hutchison, J.E.; et al. Anode Catalysts in Anion-Exchange-Membrane Electrolysis without Supporting Electrolyte: Conductivity, Dynamics, and Ionomer Degradation. *Adv. Mater.* **2022**, *34*, 2203033. https://doi.org/10.1002/adma.202203033.
83. Lim, H.; Jeong, J.; Shin, G.; Kim, C.; Choi, G.; Myeong, S.; Choi, S.M.; Park, T. Realizing Superior Durability of Water Electrolyzer Using Anion Exchange Membrane with an Interstitial Alkyl Chain: From a Single Cell to Large-Sized 1-cell Stack. *Adv. Energy Mater.* **2024**, *14*, 2401725. https://doi.org/10.1002/aenm.202401725.
84. Donker, E.J.; Potgieter, M.; Creus, J.; Wonink, M.B.S.; de Groot, M.T.; Kriek, R.J.; Seland, F.; Sunde, S. From RDE to Flowcell: The Impact of Iron on Nickel Catalyst Stability and Performance in Anion Exchange Membrane Water Electrolyzers. Electrochim. Acta 2026, 560, 148639. https://doi.org/10.1016/j.electacta.2026.148639.
85. Folkman, S.J.; Gelmetti, I.; Giancola, S.; Garcés-Pineda, F.A.; Spadaro, M.C.; Muñoz, A.C.; Wickramasinghe, T.; Arbiol, J.; Galán-Mascarós, J.R. One-Step Synthesis of Highly Active and Conductive Transition Metal Nitride for Oxygen Evolution in Alkaline Anion Exchange Membrane Electrolysis. *ACS Appl. Energy Mater.* **2026**, *9*, 5951–5960. https://doi.org/10.1021/acsaem.5c04052.
86. Lindquist, G.A.; Oener, S.Z.; Krivina, R.; Motz, A.R.; Keane, A.; Capuano, C.; Ayers, K.E.; Boettcher, S.W. Performance and Durability of Pure-Water-Fed Anion Exchange Membrane Electrolyzers Using Baseline Materials and Operation. *ACS Appl. Mater. Interfaces* **2021**, *13*, 51917–51924. https://doi.org/10.1021/acsami.1c06053.
87. Kim, M.; Nachtergaele, P.; Lee, D.; Kim, M.; Kim, J.; You, F.; Charles, M. Prospective Sustainability Assessment of Water Electrolyzer Green Hydrogen Process Systems: A Monetization-Based Approach. *Appl. Energy* **2026**, *415*, 127934. https://doi.org/10.1016/j.apenergy.2026.127934.
88. Reimonn, G.; Kamcev, J. Techno-Economic Perspective on the Limitations and Prospects of Ion-Exchange Membrane Technologies. *Curr. Opin. Chem. Eng.* **2025**, *47*, 101077.
89. Campbell-Stanway, C.; Becerra, V.; Prabhu, S. Techno-Economic Analysis with Electrolyser Degradation Modelling in Green Hydrogen Production Scenarios. *Int. J. Hydrogen Energy* **2025**, *106*, 80–95. https://doi.org/10.1016/j.ijhydene.2025.01.359.
90. James, B.D.; Acevedo, Y.M.; McNamara, K.R.; Prosser, J.H.; Huya-Kouadio, J.M. Hydrogen Production Cost with Anion Exchange Membrane Electrolysis; Technical Report; Strategic Analysis, Inc.: Arlington, VA, USA, 2024. https://doi.org/10.2172/2476013.

Disclaimer/Publisher's Note: The statements, opinions and data contained in all publications are solely those of the individual author(s) and contributor(s) and not of MDPI and/or the editor(s). MDPI and/or the editor(s) disclaim responsibility for any injury to people or property resulting from any ideas, methods, instructions or products referred to in the content.